

Durham E-Theses

Large-Scale Structure Tests of Cosmological Models

JOHNSON, ROSS,WILLIAM,FLETCHER

How to cite:

JOHNSON, ROSS,WILLIAM,FLETCHER (2015) *Large-Scale Structure Tests of Cosmological Models*, Durham theses, Durham University. Available at Durham E-Theses Online:
<http://etheses.dur.ac.uk/11001/>

Use policy



This work is licensed under a [Creative Commons Attribution 3.0 \(CC BY\)](https://creativecommons.org/licenses/by/3.0/)

Large-Scale Structure Tests of Cosmological Models

Ross W. F. Johnson

Abstract

We investigate the use of N -body simulations and large-scale galaxy clustering in order to test two cosmological models: an Einstein-de Sitter model where neutrinos act as the dominant Hot Dark Matter (HDM) component; and the standard Λ Cold Dark Matter (Λ CDM) model. We investigate the matter power spectra and halo mass functions of the neutrino model, and of an extended model that includes Primordial Magnetic Fields (PMFs), which have the effect of introducing ‘seeds’ into the matter distribution. We find that neither model performs as well as Λ CDM in generating structure, but note that the use of PMFs completely reverses the process of structure formation in the HDM model, allowing it to progress in a bottom-up manner.

We calculate the redshift-space two-point galaxy-galaxy correlation function, $\xi(s)$, of the Sloan Digital Sky Survey (SDSS) Seventh Data Release (DR7) MAIN galaxy catalogue, and fit this to both the Λ CDM model and the neutrino model. Assuming a Λ CDM cosmology, we obtain a best-fit value for the spherically averaged distance to redshift $z = 0.15$, given as $D_V(0.15) = (627 \pm 61\text{Mpc}) \left(\frac{r_s}{r_{s, fid}} \right)$. This is in agreement with recent work, and is our best-fit model to the SDSS DR7 MAIN data. We find that the correlation function from the MAIN galaxies cannot reject an $\Omega_m = 1$ model in a cosmological ruler test, and the BAO peak is not pronounced enough to significantly reject a neutrino HDM model. However, the neutrino model is rejected by the non-linear form of the matter power spectrum, even though the magnetic version of the model may form galaxies by the present day.

Large-Scale Structure Tests of Cosmological Models

Ross William Fletcher Johnson

A Thesis presented for the degree of
Master of Science by Research



Department of Physics
University of Durham
England

November 2014

Contents

Abstract	i
Declaration	vii
Acknowledgements	1
1 Introduction	2
2 Neutrino Model	4
2.1 Introduction	4
2.2 Simulation Methods	5
2.2.1 Initial Conditions	5
2.2.2 Measuring $P(k)$	8
2.2.3 Halo Mass Function	8
2.3 Results	9
2.3.1 Neutrino Model	9
2.3.2 Magnetic Neutrino Models	15
2.4 Discussion	17
3 Baryon Acoustic Oscillations	19
3.1 Introduction	19
3.2 Sample	20
3.3 Methods	20
3.3.1 Measuring the Correlation Function	20
3.3.2 Error Estimation	21
3.3.3 Cosmological Ruler	22
3.3.4 Model Fitting	23
3.4 Results	24
3.4.1 Cosmological Ruler	24
3.4.2 Parameter Exploration	25
3.4.3 Neutrino Cosmology	29

Contents	iv
3.5 Discussion	30
3.5.1 Alternate Cosmological Models	33
4 Conclusion	34

List of Figures

2.1	Theoretical temperature power spectrum for a magnetic neutrino model	5
2.2	Theoretical $z = 0$ $P(k)$ and $\Delta^2(k)$ for the neutrino models	7
2.3	Theoretical $z = 0$ $P(k)$ and $\Delta^2(k)$ for the magnetic neutrino models	7
2.4	Power spectra for the neutrino models at $z = 0$	11
2.5	Redshift-evolution of the power spectra for the neutrino models	11
2.6	Redshift-evolution of the corrected power spectra for the low-resolution neutrino models	12
2.7	Raw output of POWMES for the $z = 0$ $\sigma_8 = 0.22$ model	12
2.8	Redshift-evolution of the corrected power spectra for the neutrino models	13
2.9	Cumulative mass functions for the $\sigma_8 = 0.52$ and 0.82 models	14
2.10	Corrected cumulative mass functions for the $\sigma_8 = 0.52$ and 0.82 models	14
2.11	Redshift-evolution of the power spectra for the magnetic neutrino models	16
2.12	Redshift-evolution of the corrected power spectra for the successful magnetic neutrino models	16
2.13	Corrected cumulative mass functions for the successful magnetic neutrino models	17
3.1	$N(z)$ and $n(z)$ for the SDSS DR7 MAIN Sample	21
3.2	Error Ratios for two different subsample schemes	22
3.3	Concordance cosmology $\xi(s)$ for the SDSS DR7 MAIN Galaxy sample at $z_{eff} = 0.15$	25
3.4	Best-fit $\xi(s)$ from the cosmological ruler test	26
3.5	Chi-squared distribution of the cosmological ruler test	26
3.6	Best-fit $\xi(s)$ from the SDSS DR7 MAIN Galaxy sample for the concordance cosmology	27
3.7	Likelihood contours for concordance cosmology	28
3.8	Best-fit models for robustness checks on $\xi(s)$	29
3.9	Neutrino cosmology $\xi(s)$ for the SDSS DR7 MAIN Galaxy sample at $z_{eff} = 0.15$	30
3.10	$\xi(s)$ for this study and Ashley et al. (2014)	31
3.11	Ratio of measured $D_V(z)/r_d$ against Planck predictions for various surveys	32

List of Tables

3.1 Robustness checks performed on measurements of α and $\Omega_m h^2$ in the Λ CDM cosmology.	27
--	----

Declaration

The work in this thesis is based on research carried out at the Astronomy and Astrophysics group, the Department of Physics, England. No part of this thesis has been submitted elsewhere for any other degree or qualification and it is all my own work unless referenced to the contrary in the text.

Copyright © 2014 by Ross William Fletcher Johnson.

“The copyright of this thesis rests with the author. No quotations from it should be published without the author’s prior written consent and information derived from it should be acknowledged”.

Acknowledgements

I would like to thank Prof. Tom Shanks for providing invaluable insight and assistance throughout the duration of this project. I would also like to thank Ben Chehade and Jascha Schewtschenko for providing additional help throughout the year.

I would like to thank Matthew Chamberlin, Alison Johnson, Benjamin Maunder and Rachael Merrison for their helpful comments and for reviewing this report.

Funding for the Sloan Digital Sky Survey (SDSS) has been provided by the Alfred P. Sloan Foundation, the Participating Institutions, the National Aeronautics and Space Administration, the National Science Foundation, the U.S. Department of Energy, the Japanese Monbukagakusho, and the Max Planck Society. The SDSS Web site is <http://www.sdss.org/>.

The SDSS is managed by the Astrophysical Research Consortium (ARC) for the Participating Institutions. The Participating Institutions are The University of Chicago, Fermilab, the Institute for Advanced Study, the Japan Participation Group, The Johns Hopkins University, Los Alamos National Laboratory, the Max-Planck-Institute for Astronomy (MPIA), the Max-Planck-Institute for Astrophysics (MPA), New Mexico State University, University of Pittsburgh, Princeton University, the United States Naval Observatory, and the University of Washington.

Chapter 1

Introduction

The study of the large-scale structure of the universe, through the use of both observation and simulation, is the primary method by which we further our understanding of the fundamental aspects of the universe. Through observation of the evolution of the universe over time it is possible to formulate a description of both the origin and ultimate fate of the universe with ever increasing precision, while study of the structure of the universe at the present day can inform us of the underlying composition of the universe, and hint at exciting new physics such as Dark Matter (DM) (Zwicky 1933), or Modified Newtonian Dynamics (MOND) (Milgrom 1983). Simulations of the universe, on the other hand, serve primarily as a tool to verify and constrain various cosmological models, but can also themselves shed light on physical processes that may not otherwise be explored, such as the various feedback processes thought to occur in galaxy formation (Benson et al. 2003, Baugh et al. 2005, Bower et al. 2006).

The current standard model of the universe, dubbed the Lambda-Cold Dark Matter (Λ CDM) model, has had great success in describing the large scale structure of the universe and its evolution since cosmic inflation, accounting for effects on all astrophysical scales, from the rotation curves of galaxies (Ostriker & Peebles 1973, Ostriker, Peebles & Yahil 1974) to the observed acceleration of the expansion of the universe (Schmidt et al. 1998, Perlmutter et al. 1999). It has accurately predicted the existence of Baryon Acoustic Oscillations (BAO) in the observed distribution of galaxies (Eisenstein et al. 2005, Cole et al. 2005), an imprinting of sound waves generated in the plasma before recombination (Peebles & Yu 1970, Sunyaev & Zel'dovich 1970). It has also resolved many of the issues plaguing earlier cosmological models, such as observations of stellar ages apparently greater than the age of the universe (e.g. Chaboyer 1998). However, large parts of the model itself remain a mystery; many aspects were introduced without a firm theoretical basis (e.g. Dark Energy, gaussian initial density fluctuations), and there is difficulty in reconciling predictions at astrophysical scales to observations (e.g. overprediction of low-mass satellite galaxies (Klypin et al. 1999, Moore et al. 1999)). The two most glaring problems it faces are the lack of any detected candidate for the Cold Dark Matter particle, and the fine-tuning, to 1 part in 10^{120} , of

the cosmological constant (Weinberg 1989). Other models attempting to avoid such extensions can explain certain features better, but either sacrifice accuracy in other areas, or retain other unsavoury aspects of the Λ CDM model. MOND, for instance, accurately describes astrophysical scales, but must resort to a Λ term when describing cosmological scales (e.g. Angus 2009).

In this paper we will discuss a number of alternative models, and investigate how they perform on various scales in order to build a fuller picture of their merits and faults. Our second chapter focusses on a neutrino model proposed by Shanks et al. (2014). This is an Einstein-de Sitter model where neutrinos act as a dominant dark matter component, whose underlying principle is one of relative simplicity: as little new physics as possible. We will also discuss a possible extension to this model, in the form of primordial magnetic fields which can generate seeds that initiate structure formation. We will study the evolution over time of large-scale structure (LSS) in these models through the use of N -body simulations, and note how this differs from Λ CDM. In chapter 3 we study the large-scale structure of the observable universe in the form of galaxies out to redshift $z = 0.2$. We investigate the redshift-space correlation function of galaxies in light of both the Λ CDM and neutrino models, and discuss the capabilities of both to match observational data. Through this discussion we hope to illuminate the difficulties faced by alternative cosmological models when competing against the standard model in its home turf. Throughout this paper we use the convention $H_0 = 100 \times h \text{ km s}^{-1} \text{ Mpc}^{-1}$.

Chapter 2

Neutrino Model

2.1 Introduction

In this chapter we assume a cosmology described by $\Omega_m = 1$, $\Omega_b = 0.15$, $\Omega_\nu = 0.85$, $h = 0.45$, where neutrinos of mass $m_{\nu_e} = 5$ eV act as a Hot Dark Matter (HDM) component of the matter density of the universe. This Einstein-de Sitter model avoids some of the problems inherent in the concordance cosmology, such as the coincidence that $\rho_\Lambda \approx \rho_m$ at the present day, but comes with its own set of problems. Such a mass for neutrinos is in tension with tritium β -decay experiments, which suggest $m_{\nu_e} < 2.2$ eV (95 per cent confidence) (Aseev et al. 2011), while setting h as low as 0.45 is required in order to allow such a high $\Omega_b h^2$, but is in disagreement with a multitude of other works such as PLANCK (Planck Collaboration, Ade et al. 2014*b*) ($H_0 = 67.3 \pm 1.2$ km s⁻¹ Mpc⁻¹) or Riess et al. (2011) ($H_0 = 73.8 \pm 2.4$ km s⁻¹ Mpc⁻¹). Nonetheless, given the not insignificant difficulties faced by Λ CDM, it is worthwhile to consider a variety of alternative models. In continuation of the work by Shanks et al. (2014), we investigate how this neutrino model compares to the Λ CDM model in terms of the power spectrum and halo mass functions, through the use of N -body simulations. We also explore one of the avenues suggested by Shanks et al. to boost the normalization of the power spectrum; the introduction of seeds formed by Primordial Magnetic Fields (PMF) could provide a natural means by which to amplify structure formation in these HDM models. This is motivated in part by Wang & White (2007), who show that any seeds formed in filaments or sheets may collapse and grow rapidly, accelerating structure growth greatly. Coles (1992) suggested that PMF could provide the initial seeds of galaxies, which then triggers structure formation in a bottom-up fashion, similar to Λ CDM, earlier than the traditional HDM ‘pancake collapse’ would otherwise occur. Wasserman (1978) suggested that a PMF could have appreciable effects on the matter distribution, and Peebles (1980) further suggested that an intergalactic PMF of $B \sim 1$ nG would be enough to create a density contrast of $\delta \approx 10^{-3}$ at decoupling ($z \approx 1000$).

Inspection of a theoretical temperature power spectrum from one of the proposed models, a

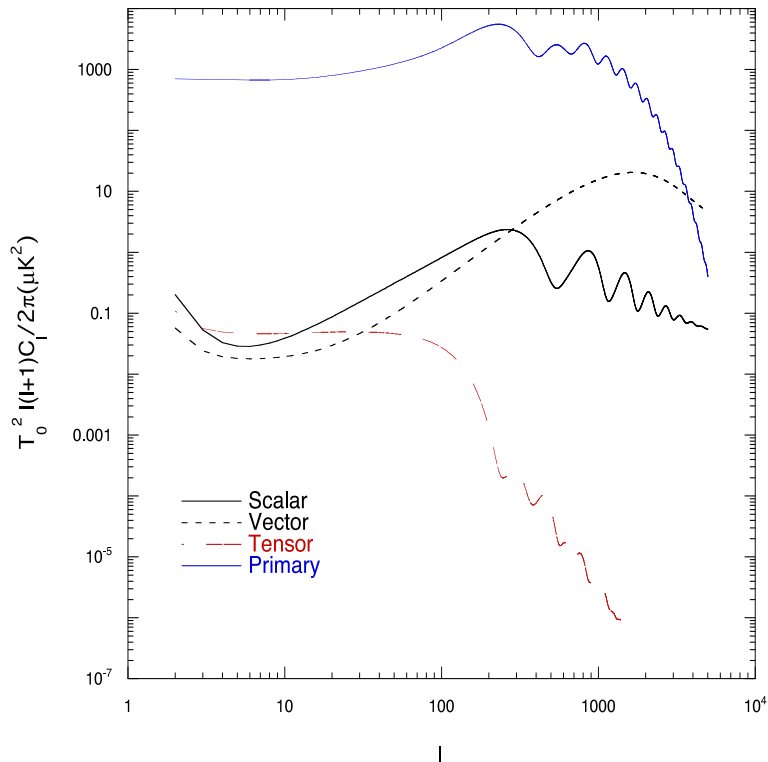


Figure 2.1: Theoretical temperature power spectrum for a magnetic neutrino model. Shown are: the base temperature power spectrum for the neutrino model (solid blue line); contributions to the temperature power spectrum from scalar modes (black solid line); contributions to the power spectrum from vector modes (black dashed line); and contributions to the temperature power spectrum from tensor modes (red long-dashed line).

model with $n_B = 2.9$, demonstrates that the addition of a compensated magnetic field introduces scalar, vector and tensor modes (see Fig. 2.1). With the assumed magnetic field strength of $B_\lambda = 4.7$ nG, these additional modes are at too low an amplitude to be excluded by the CMB temperature power spectrum.

This chapter is organised as follows: we describe the N -body simulations, and the analysis performed in § 2.2; we present the results of our analyses for our neutrino models, followed by our magnetic models, in § 2.3; finally, we present a discussion of our results in § 2.4.

2.2 Simulation Methods

2.2.1 Initial Conditions

We make use of the Tree-SPH code GADGET-2 (Springel 2005) to carry out our N -body simulations. We use $N_{part} = 2 \times 256^3$ particles in our simulations, and use boxes of size $L = 150 h^{-1}$ Mpc to probe the halo mass function and power spectrum at different scales. In addition to these simulations, we perform two other sets: a set of simulations with $N_{part} = 2 \times 128^3$ to check

for the presence of numerical artefacts in our neutrino simulations; and a set of simulations with $L = 50 h^{-1}$ Mpc, to constrain the power spectra and mass functions of the magnetic model simulations at small scales. We begin all simulations at $z = 7$, and apply perturbations to an initial glass configuration of particles.

Unphysical perturbations in density can occur if additional thermal velocities are applied to the initial conditions, although the exact mechanism of generation is unclear. These are increasingly problematic the earlier the simulations are begun (e.g. Power 2013, Colín et al. 2008), as the magnitude of the additional thermal velocities approaches the free streaming velocity, and we find that even starting our simulations at $z = 7$ with free-streaming produces these spurious features. We therefore do not include free-streaming in our models, instead treating neutrinos as collisionless dark matter.

The perturbations applied to our initial load are calculated according to the Zel'dovich approximation from an initial power spectrum generated by the boltzmann code CAMB (Lewis, Challinor & Lasenby 2000), suitably modified where required to account for magnetic seed generation (Shaw & Lewis 2010). These modifications provide, in addition to the base power spectrum, the contributions due to the magnetic field power spectrum, defined as

$$P_B(k) = Ak^{n_B}, \quad (2.1)$$

where A is some amplitude term dependent on the variance of the magnetic field strength, B_λ^2 , on scales $\lambda = 1$ Mpc:

$$A = \frac{(2\pi)^{n_B+5} B_\lambda^2}{2\Gamma\left(\frac{n_B+3}{2}\right) k_\lambda^{n_B+3}}. \quad (2.2)$$

We investigate the effects of 3 values of n_B on the matter power spectra: $n_B = -2.0, -2.9$ and -3.3 , with $B_\lambda = 4.7$ nG.

For our non-magnetic models we run additional simulations with renormalized $P(k)$ in order to see the minimum increase required to allow structure to form. We do this by increasing σ_8 , the mass variance in spheres of radius $8 h^{-1}$ Mpc used to normalize $P(k)$, from 0.22 to 0.52 and 0.82.

We plot our matter power spectra, along with $\Delta^2(k) \propto k^3 P(k)$, in Figs. 2.2 and 2.3. The dashed horizontal line on the plots of $\Delta^2(k)$ denote $\Delta^2(k) = 1$, which signifies order unity density perturbations, and thus the onset of spherical collapse for wavenumbers about k . All magnetic spectra exceed $\Delta^2(k) = 1$ by the present day, and hence do not require renormalization, but even the renormalized neutrino-only power spectra remain less than 1. These models must therefore undergo some other non-linear processes in order to produce structure by the present day, but this is expected given that structure in these models forms from the top down, and not due to the spherical collapse model as in Λ CDM.

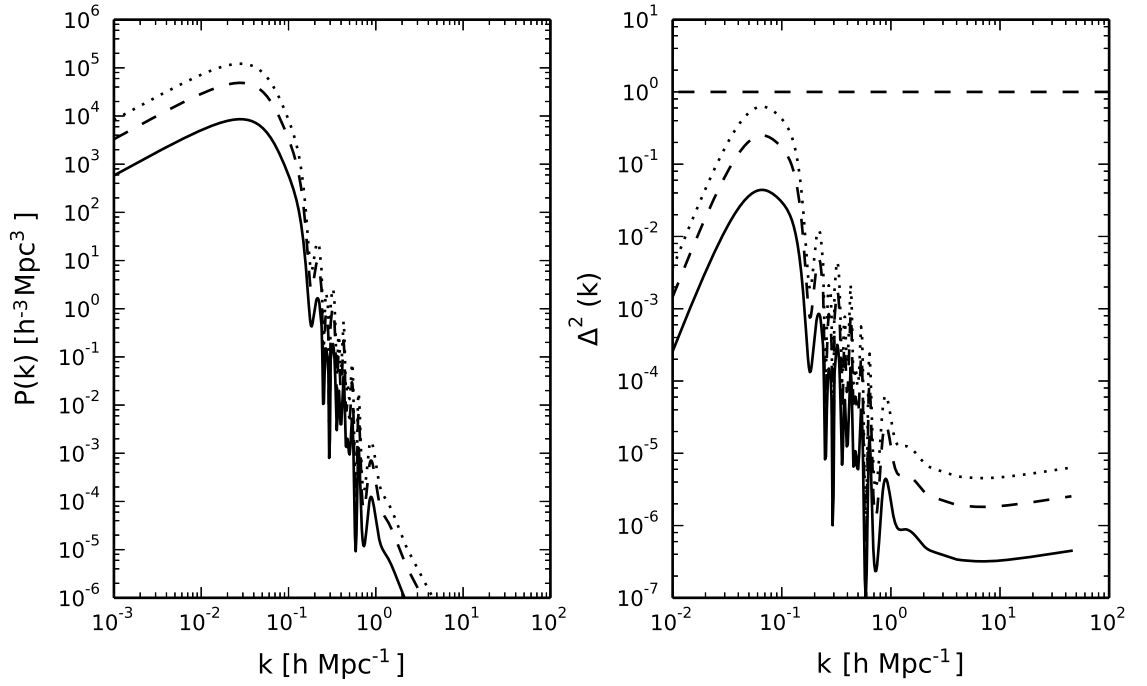


Figure 2.2: Theoretical $z = 0$ $P(k)$ (left panel) and $\Delta^2(k)$ (right panel) for the neutrino models. Shown are spectra normalized to: $\sigma_8 = 0.22$ (solid line); $\sigma_8 = 0.52$ (dashed line); and $\sigma_8 = 0.82$ (dotted line). The horizontal dashed line in the $\Delta^2(k)$ plot denotes $\Delta^2(k) = 1$.

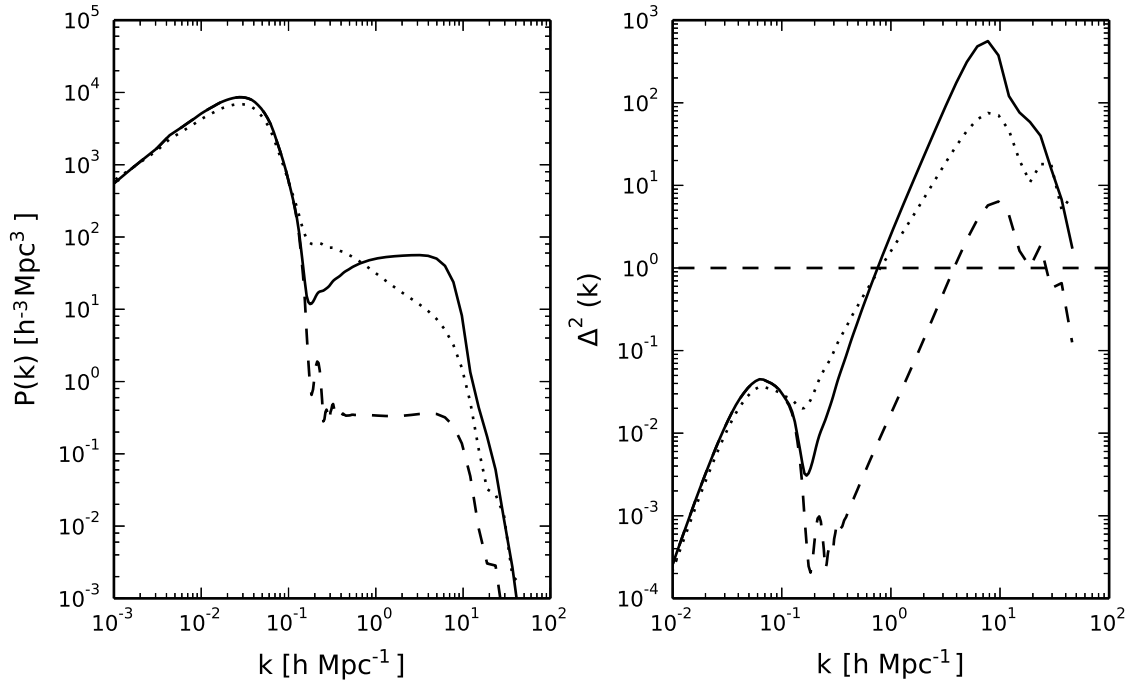


Figure 2.3: Theoretical $z = 0$ $P(k)$ (left panel) and $\Delta^2(k)$ (right panel) for the magnetic neutrino models. Shown are spectra with: $n_B = -2.0$ (solid line); $n_B = -2.9$ (dashed line); and $n_B = -3.3$ (dotted line). The horizontal dashed line in the $\Delta^2(k)$ plot denotes $\Delta^2(k) = 1$.

2.2.2 Measuring $P(k)$

We make use of the free program POWMES¹ (Colombi et al. 2009) to calculate our power spectrum for our simulation outputs. POWMES measures the power contained in fourier modes of multiples of $2\pi/L$, and gives as output $P_{rough}(k)$,

$$P_{rough}(k) = P_V(k) + \frac{1}{N_{part}}, \quad (2.3)$$

where $P_V(k) = P(k)/L^3$, and $1/N_{part}$ is the systematic shot noise contribution from the discrete nature of the simulations. This correction is unnecessary when analysing the spectra of the initial conditions, as these are essentially still a perturbed glass. POWMES also provides an estimate of the fractional errors on $P_{rough}(k)$ due to the finite number of modes per k bin:

$$\left(\frac{\Delta P_{rough}(k)}{P_{rough}(k)}\right)^2 = \frac{1}{C(k)}, \quad (2.4)$$

which translates to fractional errors on the shot-noise corrected $P_V(k)$ as

$$\left(\frac{\Delta P_V(k)}{P_V(k)}\right)^2 = \frac{1}{C(k)} \left(1 + \frac{2}{N_{part}P_V(k)} + \frac{1}{(N_{part}P_V(k))^2}\right), \quad (2.5)$$

where this wavenumber discreteness is taken into account by the $C(k)$ term. There are two other sources of systematic error, both arising from the process of Taylor expansion in the code. The first of these is due to the order of the Taylor expansion, taken into account within the code itself. The final source stems from imposing a grid upon the particle distribution in order to calculate the fast-fourier transform, and makes itself manifest when the Nyquist frequency of the grid, k_{Ny} , is approached. We limit our probing of $P(k)$ to wavenumbers below $k_{Ny}/2$, thus avoiding this problem, although this scale is above what can be probed accurately due to the resolution of our simulations.

2.2.3 Halo Mass Function

We use the Friends-of-Friends (FoF) algorithm to identify collapsed structures in our simulations. This identifies particles within some distance b of the mean interparticle spacing as belonging to the same halo, although this can result in unspherical halos, and some overestimation of the masses of small halos. To remedy this we apply the correction to the number of particles in a halo, N_H , derived by Warren et al. (2006):

$$N_{H,corr} = N_H (1 - N_H^{0.6}). \quad (2.6)$$

This assumes $b = 0.2$, which we therefore use in our identification process. The halos we find are all of a single particle type, and so we apply an additional correction to the masses of the halos to account for the missing particle species. This is given by

¹Available for free at www.projet-horizon.fr

$$M_H = M_{DM} \frac{\Omega_m}{\Omega_m - \Omega_b}, \quad (2.7)$$

where M_{DM} is the mass of the dark matter-only halos.

Wang & White (2007) discussed the formation of unphysical halos in HDM simulations due to discreteness in the simulations. The mechanism for the production of these features is unclear, but it appears that at multiples of the mean interparticle spacing small, unphysical perturbations form that act as seeds for the formation of larger halos. The authors propose a lower limit for the mass of halos that can be confidently assumed to be ‘true’ halos, given by

$$M_{lim} = 10.1 \times \bar{\rho} d k_{peak}^{-2}, \quad (2.8)$$

where d is the mean interparticle spacing, and k_{peak} the wavenumber at which $\Delta^2(k)$ is maximum. They determine the factor 10.1 for their own HDM model, and suggest that this may depend upon the exact shape of the power spectrum; in the absence of a rigorous formulation of this dependence we find this factor suffices for our models too. This can be used as a hard lower-limit on the masses of halos found in the simulation, but Schneider et al. (2013) interpret this instead as a lower bound, below which unphysical halos dominate. They argue that the mass function may still be probed below this scale, if one can subtract the contribution from these numerical artefacts. They therefore apply a power law fit to those halos that clearly (by visual inspection) lie above M_{lim} , and subtract this fit from the entire mass function. This produces the characteristic downturn at low masses expected in hot or warm dark matter models. We use this method in our investigations into the halo mass function for our neutrino models, however, we must note that we have extrapolated the form of this correction to larger masses in order to apply it. This therefore reduces the amplitude at intermediate scales, but all salient features are retained (as shown in their fig. 4). We do not apply this method to our magnetic models, as $\Delta^2(k) > 1$ by the present day.

2.3 Results

In this section we detail the main results of our investigations. We begin by considering the power spectra and halo mass functions recovered from our neutrino simulations, which we compare to $z = 0$ Λ CDM predictions, and study their evolution over time. We perform this same analysis for our three magnetic seed models.

2.3.1 Neutrino Model

Power Spectra

We show the $z = 0$ power spectra recovered from our neutrino simulations, alongside both Λ CDM and theoretical predictions from CAMB for comparison, in Fig. 2.4. We note that as the

normalization of the initial neutrino spectrum is increased, the deviations from the expected $z = 0$ spectra at high- k also increase. We attribute this increase in power to non-linear effects, and also note that the power spectrum of the $\sigma_8 = 0.22$ model drops below zero after $k = 0.3 h \text{ Mpc}^{-1}$, indicating that this simulation remains essentially an unperturbed glass. As the theoretical $z = 0$ $\Delta^2(k)$ remains well below one at all scales, we remain unsurprised that the final simulation does not differ significantly from the initial conditions.

In the three panels of Fig. 2.5 we plot the redshift-evolution of the spectra for each individual model, with errors given by eqs. 2.4 and 2.5 denoted by the shaded areas, alongside the predicted $P(k)$ from CAMB. We note that as the normalization of each spectrum is increased, the deviations from the expected $z = 0$ spectra at high- k also increase. This effect begins earlier in each model, with $z = 2$ exhibiting small non-linear effects in the $\sigma_8 = 0.82$ model. For all models, $P(k)$ drops below zero after $z = 7$, and only the $\sigma_8 = 0.82$ model remains above zero for all measured k at $z = 0$. This suggests that all models remain essentially unperturbed glasses after $z = 7$, with only the two higher-normalized models deforming appreciably by redshift $z = 0$. As such, we will not apply the $1/N_{part}$ corrections to all models for $z > 0$, and for the $\sigma_8 = 0.22$ model for all redshifts.

The discontinuities observed at $k = 2.68 h \text{ Mpc}^{-1}$ appear to be numerical artefacts, as they occur in each model. In order to test this, we perform the same simulations with $N_{part} = 128^3$. In Fig. 2.6 we show the lower resolution $P(k)$, which displays the same upturns at the same locations, suggesting instead an error in the POWMES code. We plot the raw output of POWMES for the $z = 0$, $\sigma_8 = 0.22$ simulations, as well as output from POWMES with $k_{max} = 1024$, and with the resolution of the fast-fourier transform grid set to 300 (from 512 and 256 respectively), in Fig. 2.7. We find that changing k_{max} has no effect on the discontinuity, but changing the resolution of the grid changes the wavenumber of this discontinuity from $kL/2\pi = 64$ to 75; this is a numerical error arising from the fast-fourier transform applied in POWMES, and not due to either the initial conditions, or GADGET-2. We conclude that POWMES results cannot be trusted for integer wavenumbers greater than a quarter of the resolution of the grid for these models, and so we will exclude them from our results.

We present the final $P(k)$ for the neutrino models, with $1/N_{part}$ corrections withheld as discussed above, in Fig. 2.8. The increasing non-linearity as the normalization is increased is now readily apparent, and we also observe a smoothing of $P(k)$ in all models, suggesting the start of some non-linear processes. These effects are far too small to suggest the presence of structure, however, and so we do not expect to find structure in any model earlier than $z = 1$, and certainly not in the $\sigma_8 = 0.22$ model. The upturns just before $kL/2\pi = 64$ seem to be related to the discontinuities mentioned earlier, but as the scale at which they begin ($kL/2\pi = 29$) is unrelated to the resolution of the fast-fourier transform grid, we include these wavenumbers.

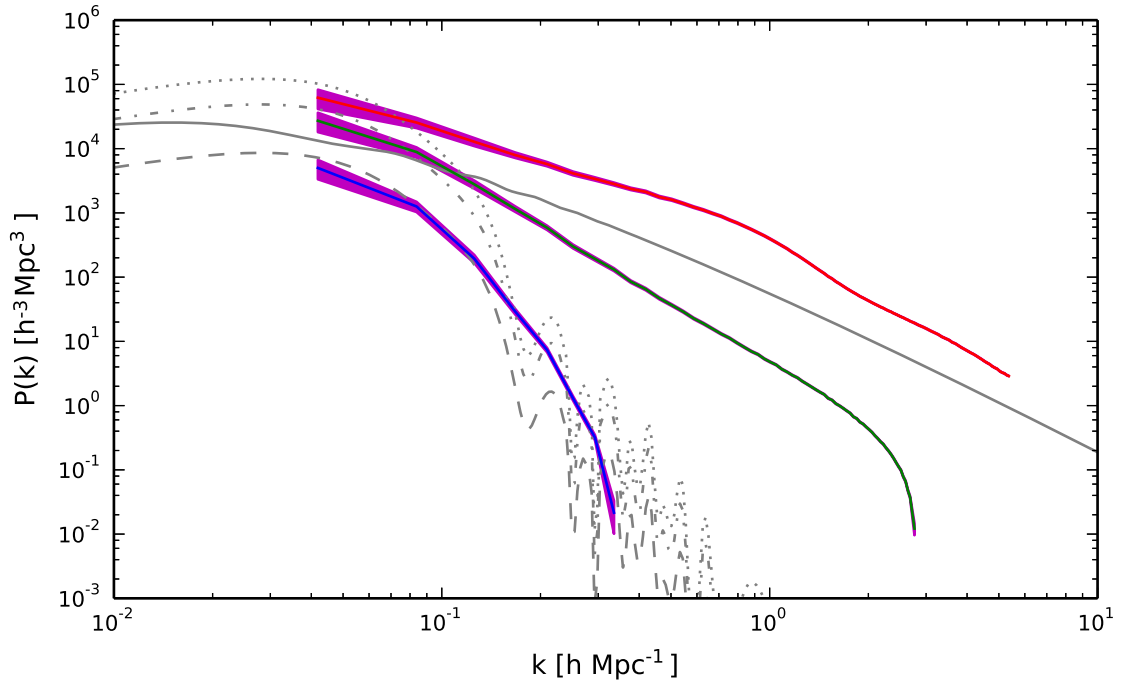


Figure 2.4: The $z = 0$ $P(k)$ of the three neutrino models, alongside theoretical spectra, in grey. The recovered $P(k)$ are shown as the solid, coloured lines, and are from top to bottom: $\sigma_8 = 0.82$, $\sigma_8 = 0.52$ and $\sigma_8 = 0.22$. Theoretical spectra from correspond to CAMB predictions, and are: Λ CDM (solid); $\sigma_8 = 0.22$ (dashed); $\sigma_8 = 0.52$ (dot-dashed); and $\sigma_8 = 0.82$ (dotted). Errors on the measured $P(k)$ are the shaded grey areas about the solid lines.

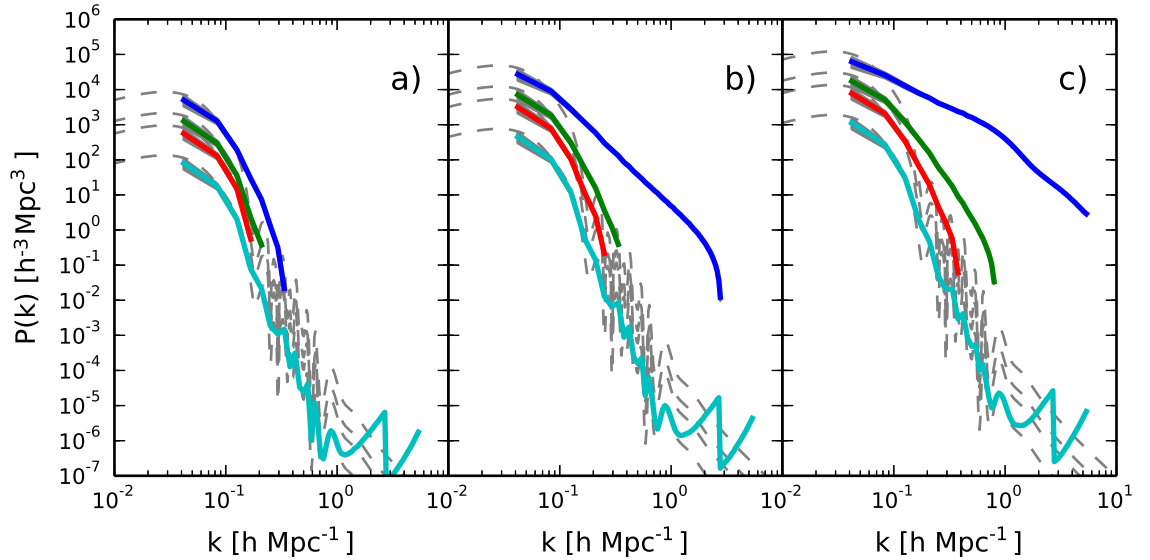


Figure 2.5: The redshift-evolution of the three neutrino models: a) $\sigma_8 = 0.22$; b) $\sigma_8 = 0.52$; c) $\sigma_8 = 0.82$. Recovered $P(k)$ are shown as the solid lines, and from top to bottom in each figure, the redshifts displayed are $z = 0, 1, 2$ and 7 . Theoretical spectra from CAMB are shown as the dashed, grey lines, and errors on the measured $P(k)$ are the shaded grey areas about the solid lines.

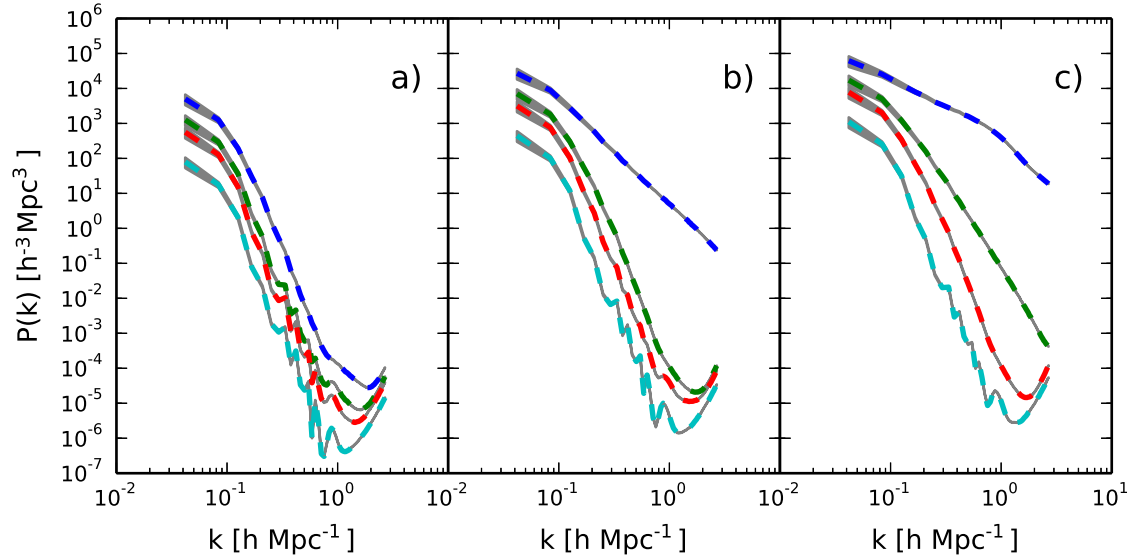


Figure 2.6: As Fig. 2.5, but for the low-resolution simulations. Particle distributions are treated as the initial loads in all models for $z > 0$, and for the $\sigma_8 = 0.22$ model for all redshifts.

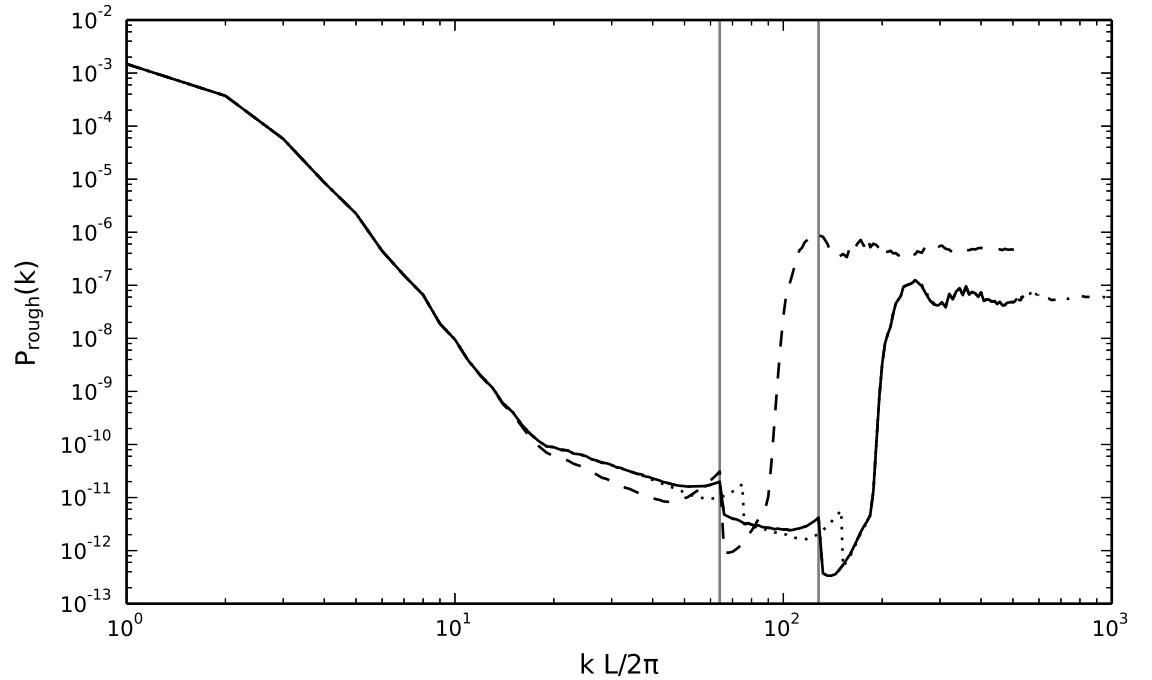


Figure 2.7: The raw output of POWMES, $P_{rough}(k)$, for the $z = 0$ $\sigma_8 = 0.22$ model. The spectra displayed correspond to: a simulation with $N_{part} = 256^3$ particles (solid line); a simulation with $N_{part} = 128^3$ particles (dashed line); the output from POWMES with $k_{max} = 1024$ (dot-dashed line); and the output from POWMES with the fast-fourier transform grid resolution set to 300 (dotted line). We also display the the Nyquist frequencies of the two simulations as grey vertical lines.

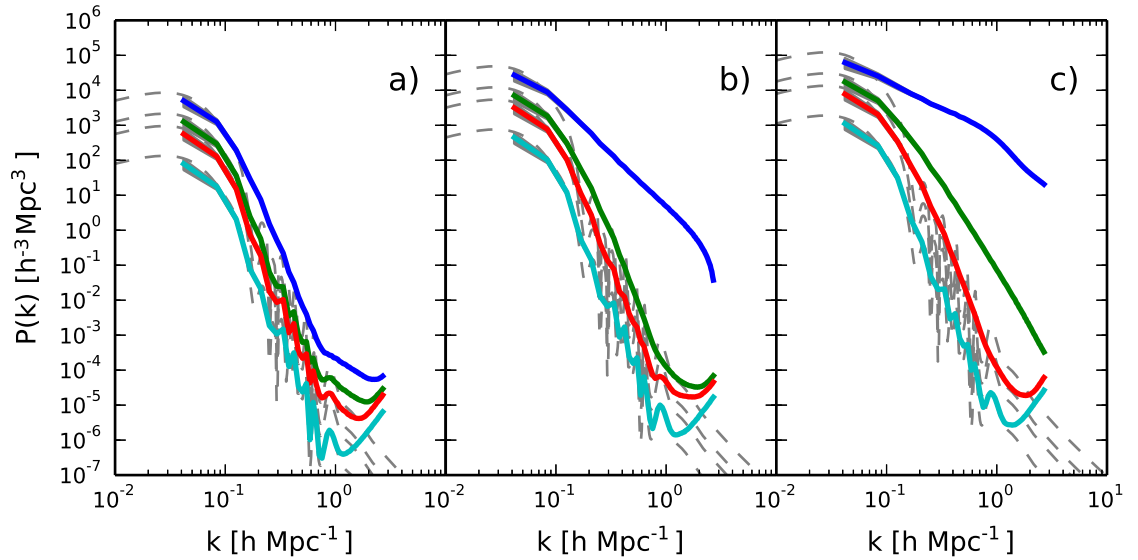


Figure 2.8: As Fig. 2.5, but with particle distributions treated as the initial loads in all models for $z > 0$, and for the $\sigma_8 = 0.22$ model for all redshifts. $P(k)$ is displayed up to $kL/2\pi = 64$, as POWMES introduces errors from the fast-fourier transform grid below this scale.

Halo Mass Function

We present the recovered cumulative mass functions from our simulations in Fig. 2.9. We have applied corrections for the FoF method and the single particle-species halos, as discussed in § 2.2.3, and display the mass functions corrected for the presence of unphysical halos separately in Fig. 2.10. The grey solid lines represent the Jenkins et al. (2001) predictions for a Λ CDM model, plotted for reference. Structure formation in all models begins late, and follows the characteristic HDM trend of increased large-scale structure and lack of small scale structure relative to Λ CDM. The presence of a large plateau suggests that very little structure is present between the scale M_{lim} , given by Eq. 2.8, and a mass scale characteristic of the cosmology. The $\sigma_8 = 0.52$ model in particular displays two large steps at high masses, which suggests that very little structure has formed even at these scales. The majority of structures found, in fact, seem to consist of those unphysical halos found at low masses, although those found at high masses are unlikely to arise from numerical processes, and so we can be sure that true structure formation has commenced.

The low-mass cut-off scale is $M_{lim} = 1.5 \times 10^{-13} h^{-1} M_\odot$ for $N_{part} = 128^3$ and $M_{lim} = 3.0 \times 10^{-13} h^{-1} M_\odot$ for $N_{part} = 256^3$. This correction has successfully removed the low-mass upturn, although some small fluctuations remain in the $N_{part} = 256^3$ simulation of the $\sigma_8 = 0.82$ model; this creates a discrepancy at the low-mass end of the downturn, but the mass functions from the two different resolutions are otherwise in agreement.

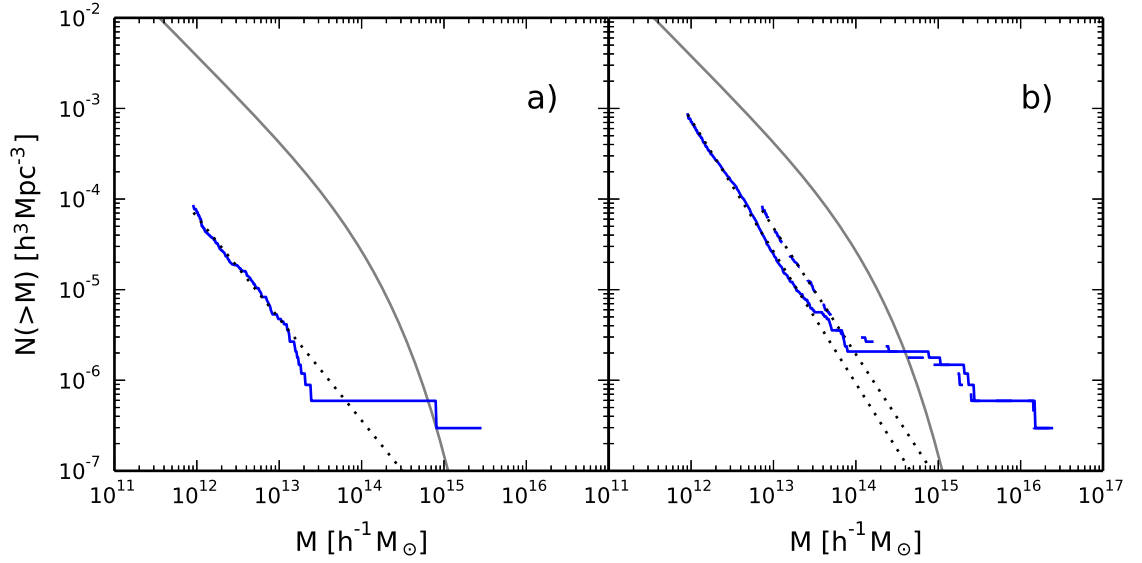


Figure 2.9: The cumulative mass functions for the two models that produced structure by $z = 0$: a) $\sigma_8 = 0.52$; and b) $\sigma_8 = 0.82$. Solid lines show simulations with $N_{part} = 128^3$, and dashed show $N_{part} = 256^3$, while dotted lines show power-law fits to the upturn at low scales. The grey solid line represents the Jenkins et al. (2001) predictions for a Λ CDM model.

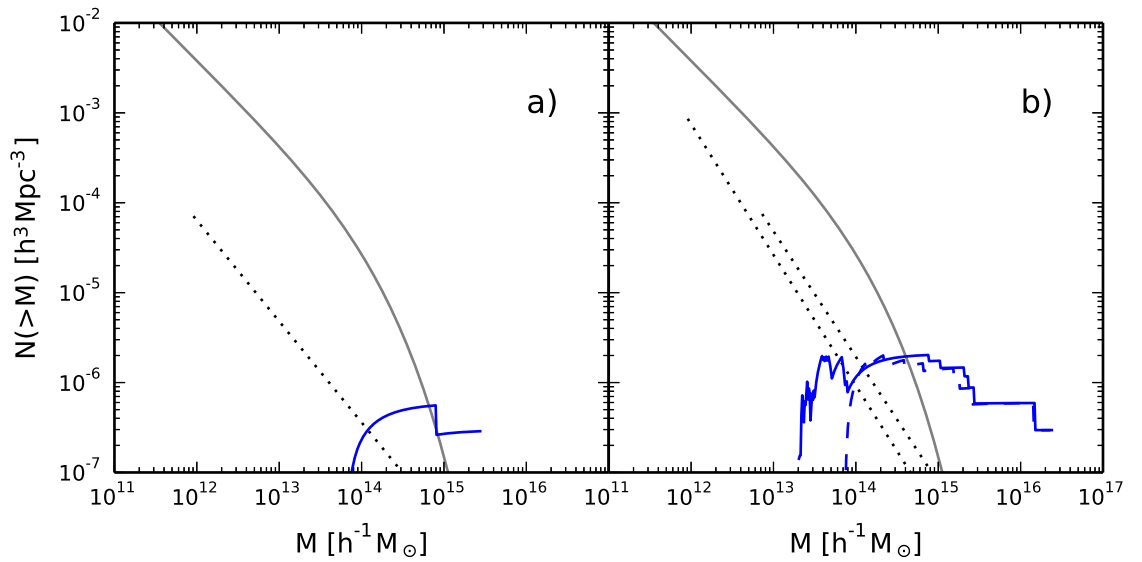


Figure 2.10: The cumulative mass functions for the two models that produced structure by $z = 0$, corrected for the presence of numerical artefacts as described in § 2.2.3. Solid lines show simulations with $N_{part} = 128^3$, and dashed show $N_{part} = 256^3$, while dotted line show power-law fits to the upturn at low scales from the uncorrected mass functions. The grey solid line represents the Jenkins et al. (2001) predictions for a Λ CDM model.

2.3.2 Magnetic Neutrino Models

Power Spectra

Fig. 2.11 shows the same as Fig. 2.5 for the magnetic $P(k)$, for $L = 150 h^{-1}$ Mpc and $50 h^{-1}$ Mpc boxes. We observe some deviation from the theoretical spectra at higher wavenumbers for the $n_B = -2.0$ model. These persist in the smaller box, suggesting that this is a ‘true’ physical effect. We note, however, that these discrepancies are also present in the initial conditions $P(k)$. We believe that this is due to some error while generating the initial conditions for this model. We will not discuss this model further, as any conclusions drawn from inspection of either the recovered $P(k)$ or the HMF would be meaningless.

We also observe deviations from theoretical predictions in the $n_B = -2.9$ model in the larger box. The initial conditions spectra are the exceptions; as the initial conditions are essentially a slightly perturbed glass, the $1/N_{part}$ correction is not applicable. Removing this correction from the later spectra improves the agreement between the two box sizes significantly, as as Fig. 2.12 shows. We conclude from this that these later snapshots are still little more than perturbed glasses, and as such, we do not discuss the HMF from this box size for this model. We observe no discontinuities such as those discussed above in any $P(k)$ presented here, and so show wavenumbers up to the Nyquist frequency of the simulation.

We note that the recovered $P(k)$, after corrections have been applied, all match the theoretical predictions well, which suggests that no non-linear structure formation has occurred. Rather, any growth of structure can be adequately described by linear growth of the initial seeds introduced by the primordial magnetic fields.

Halo Mass Function

The redshift-evolution of the cumulative mass functions recovered from the magnetic neutrino models are shown in Fig. 2.13. As discussed, we do not apply the power law correction to these models as $\Delta^2(k) = 1$ is expected to occur by at least the present day. We also only present mass functions for simulations whose power spectra we are sure of, as discussed in § 2.3.2.

The mass functions recovered from all magnetic models have a much steeper gradient than concordance cosmology, and display an excess of structure at the low-mass end. Due to the presence of the initial magnetic seeds the HMF is a lot smoother, not showing any of the traditional features of a HDM model. It is interesting to note that the mass functions at $z = 2$ and 1 for the $n_B = -3.3$ model converge at $M_h \approx 3 \times 10^{10} h^{-1} M_\odot$. We take this to be the scale that the seeds produced by the primordial magnetic fields form. Due to the presence of mergers, the $z = 0$ mass function drops below the earlier mass functions at these scales, and we also find a reduced amount of large-scale structure with respect to these neutrino models (cf. Fig. 2.9). This, coupled with the lack of any plateau, suggests that all structure formation has proceeded in a bottom-up manner, as in Λ CDM.

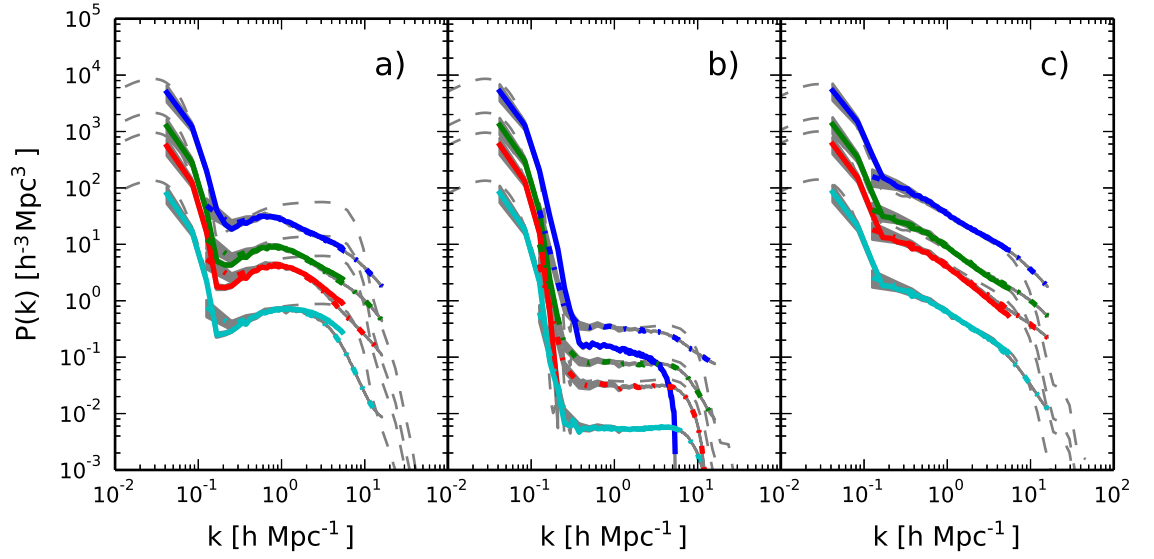


Figure 2.11: The redshift-evolution of the three magnetic neutrino models: a) $n_B = -2.0$; b) $n_B = -2.9$; c) $n_B = -3.3$. Recovered $P(k)$ are shown as the solid lines ($L = 150 h^{-1} \text{ Mpc}$), and dot-dashed lines ($L = 50 h^{-1} \text{ Mpc}$), and from top to bottom in each figure the redshifts displayed are $z = 0, 1, 2$ and 7 . Theoretical spectra from a suitably modified version of CAMB are shown as the dashed, grey lines, and errors on the measured $P(k)$ are the shaded grey areas about the solid and dot-dashed lines.

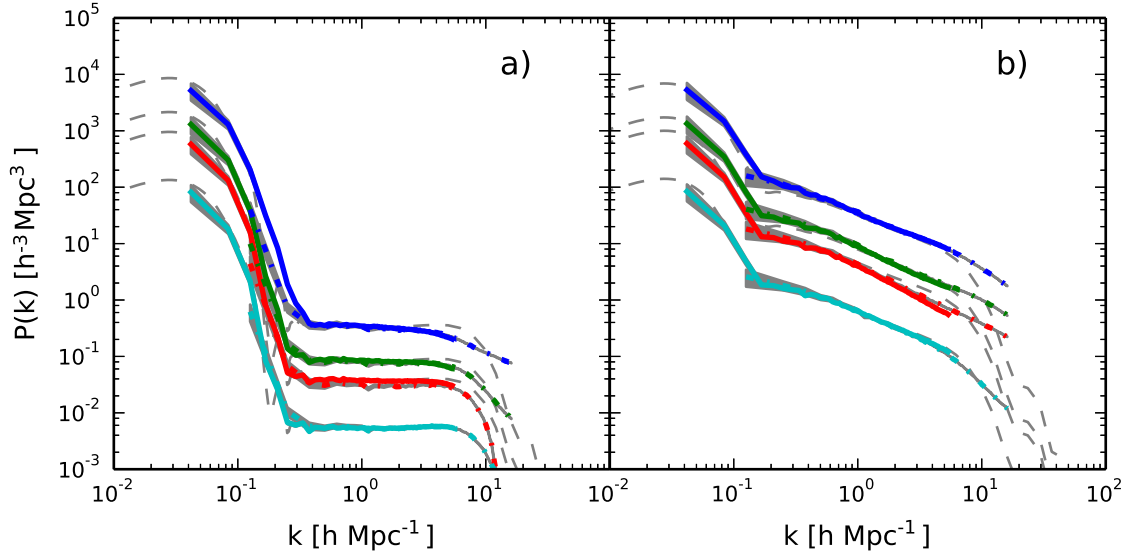


Figure 2.12: The redshift-evolution of the corrected power spectrum for the two successful magnetic neutrino models: a) $n_B = -2.9$; and b) $n_B = -3.3$. Recovered $P(k)$ are shown as the solid lines ($L = 150 h^{-1} \text{ Mpc}$), and dot-dashed lines ($L = 50 h^{-1} \text{ Mpc}$), and from top to bottom in each figure the redshifts displayed are $z = 0, 1, 2$ and 7 . Theoretical spectra from a suitably modified version of CAMB are shown as the dashed, grey lines, and errors on the measured $P(k)$ are the shaded grey areas about the solid and dot-dashed lines.

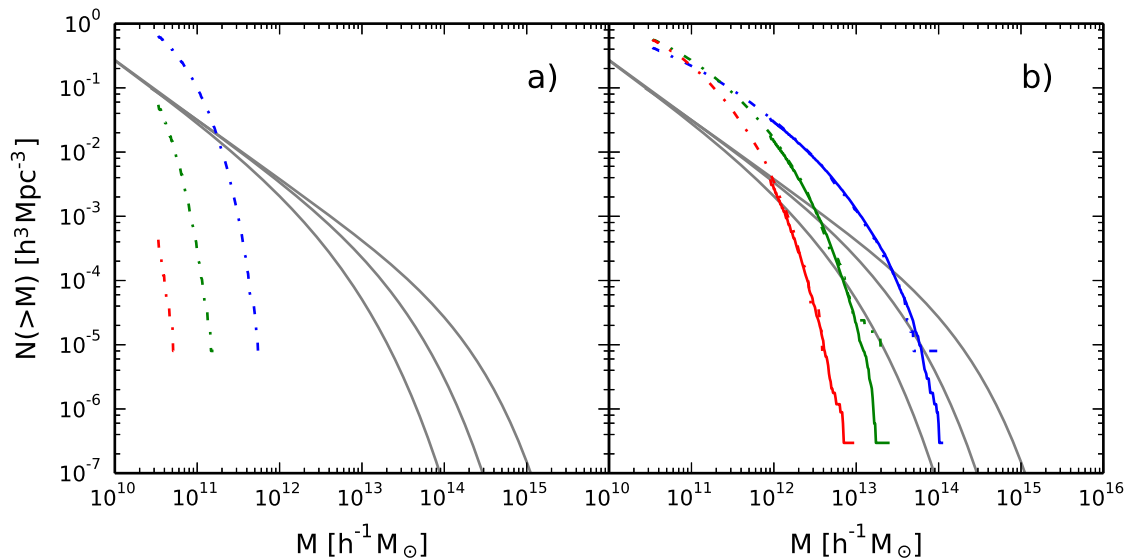


Figure 2.13: The redshift-evolution of the cumulative mass functions for the two successful magnetic neutrino models: a) $n_B = -2.9$; and b) $n_B = -3.3$. Solid lines show simulations with $L = 150 h^{-1} \text{ Mpc}$, and dot-dashed show $L = 50 h^{-1} \text{ Mpc}$. The grey solid lines represents the Jenkins et al. (2001) predictions for a ΛCDM model. The mass functions displayed are for redshifts $z = 0, 1$ and 2 , from top to bottom.

2.4 Discussion

The power spectra presented in Figs. 2.5 and 2.4 for the un-normalized models can all be described well by linear predictions until late times; the earliest noticeable non-linear behaviour is observed at redshift $z = 1$ in the $\sigma_8 = 0.82$ model. This is supported by the mass functions (Fig. 2.10), which do not show structure earlier than $z = 0$ for all neutrino models. In fact, as the structure found is primarily spurious for both models that do display it, it would seem that all non-linearities expressed in the power spectra are due to this unphysical excess.

This is problematic for the models, as the driving principle behind them is ‘what you see is what you get’, but without aid they fail to produce appreciable amounts of structure before the present day, and what they do produce is very sparse indeed. With quasars, for example, observed reliably past $z = 2$ (e.g. Pâris et al. 2012), this effectively rules out these models as valid descriptions of the observed universe.

The neutrino models fare better in comparison: the introduction of seeds generated by the PMF has caused structure formation to proceed in a bottom-up manner, as in ΛCDM . All structure produced seems to be a true product of the models, in that there are no observed preferred scales that scale with resolution. Contrary to the results of Kahniashvili et al. (2013), we find that the inclusion of PMF has increased the quantities of low-mass halos observed in these models, which agrees with predictions from e.g. Shaw & Lewis (2012), or Coles (1992). This is due to the fact that this is a HDM model; while including magnetic fields may have the effect of increasing the

critical overdensity needed for spherical collapse (Shibusawa et al. 2014), the seeds introduced by the PMF still generate far more structure at lower masses than seen in a typical HDM model.

The increased number of lower-mass halos with respect to Λ CDM is problematic, as Λ CDM by itself already overpredicts abundances of low-mass galaxies. The lower quantities of high-mass halos formed is also troublesome, as these fall behind even Λ CDM predictions for lower redshifts. The HMF of the $n_B = -2.9$ model certainly shows too few large mass structures to be a true competitor with the Λ CDM model, and while the $n_B = -3.3$ model is a closer match to Λ CDM, the more extreme low-mass end of the HMF is its ultimate let-down. In the end, these models are affected too strongly by the flaws inherent in a bottom-up picture of structure formation, although the fact that these HDM models have been coaxed into generating structure without any major compromises to the basic premise can be viewed as a limited success.

Chapter 3

Baryon Acoustic Oscillations

3.1 Introduction

The Sloan Digital Sky Survey (SDSS) is now in its fifteenth year and fourth iteration, and in that time has imaged more than a third of the sky in unprecedented detail, obtaining detailed information on the Milky Way, extragalactic supernovae, and galaxies and quasars out to redshift $z = 3.5$ (Frieman et al. 2008, Eisenstein et al. 2011). The catalogue of galaxies created by the SDSS has been used extensively to investigate structure on the largest scales in a bid to develop and constrain the underlying cosmological model describing the universe.

More recently, the Baryon Oscillation Spectroscopic Survey (BOSS) (Dawson et al. 2013) was explicitly assigned the task of probing the large-scale structure of galaxies in an effort to detect the BAO signal in the real- and fourier-space matter distribution. They have published results from three data releases of the SDSS, and have detected the BAO feature at greater than 7σ in their 11th Data Release (Anderson et al. 2014a). This is a striking success, and they have made extensive use of a variety of techniques in order both to improve the signal-to-noise ratio of their data and to quantify the errors in their measurements in order to prove the robustness and accuracy of their result.

Previous surveys have also had success in detecting the BAO feature. The seventh data release (DR7) (Abazajian et al. 2009) of the SDSS in particular had great success when combining the magnitude limited, low-redshift MAIN galaxy sample with the higher redshift, near-volume limited Luminous Red Galaxy (LRG) sample. Percival et al. (2010) detected the BAO in the power spectrum of this combined dataset, and subsequent work on the DR7 data has confirmed the detection in both the power spectrum and the correlation function (e.g. Chuang, Wang & Hemantha 2012, Chuang & Wang 2013). New York University keeps a catalogue of this data release, the New York University Value Added Catalogue (NYU-VAGC)¹ (Blanton et al. 2005, Padmanabhan et al. 2008), specifically designed to facilitate investigations of galaxy formation and evolution, and

¹available at <http://sdss.physics.nyu.edu/vagc/>

providing spectroscopic and photometric data covering 10,417 deg² of the sky. We will make use of this catalogue to conduct our own study of the DR7 MAIN galaxy sample, searching for the BAO feature in redshift-space correlation function of this sample, and testing our neutrino model discussed in chapter 2 against observational data.

This chapter will be organised as follows: we first detail the particulars of our galaxy sample and the methods we use to study the correlation function in § 3.2 and 3.3, respectively; we then present the results from both our BOSS DR11 error investigation and our correlation function in § 3.4, and conclude this chapter with a discussion of the work carried out and the cosmological implications of the results presented in § 3.5.

3.2 Sample

The samples held by NYU-VAGC have been constructed specifically to facilitate investigation of galaxy clustering statistics, including galaxies out to $z \approx 0.5$ selected by various criteria described in full in Blanton et al. (2005). We make use of their ‘safe0’ data sample, which is characterised by a Petrosian r -band magnitude range of $14.5 < r < 17.6$, and accounts for fibre collisions by applying the redshift of the nearest neighbour. We further truncate this sample by selecting galaxies only from the central footprint region, in order to provide a contiguous region for study, and bounded by $z < 0.20$. This selection has a median redshift of 0.09, and a total area of 5790 deg². $N(z)$ and $n(z)$ are shown for our sample in Fig. 3.1, where $n(z) = dN(z)/dV$ and dV is the comoving volume element.

3.3 Methods

We detail below the methods used to estimate the correlation function of the SDSS DR7 MAIN galaxy sample. We also outline the analysis we perform on the extracted correlation function. We assume a fiducial cosmology of $\Omega_m = 0.273$, $\Omega_b = 0.040$, $\Omega_\Lambda = 0.727$ and $H_0 = h \times 100 \text{ km s}^{-1} \text{ Mpc}^{-1}$, $h = 1$ in order to convert angular positions and redshifts into comoving distances.

3.3.1 Measuring the Correlation Function

We compute the spherically averaged two-point redshift-space correlation function, $\xi(s)$, by summing pair counts in bins of width $10 h^{-1} \text{ Mpc}$, centered on values between $15 h^{-1} \text{ Mpc}$ and $195 h^{-1} \text{ Mpc}$ inclusive. We make use of the Landy-Szalay estimator (Landy & Szalay 1993) to estimate the correlation function,

$$\xi(s) = \frac{1}{RR(s)}(DD(s) - 2DR(s) + RR(s)), \quad (3.1)$$

where $DD(s)$, $DR(s)$ and $RR(s)$ are the normalized data-data, data-random and random-random pair-counts from our sample. Random catalogues are provided by NYU-VAGC for each sample,

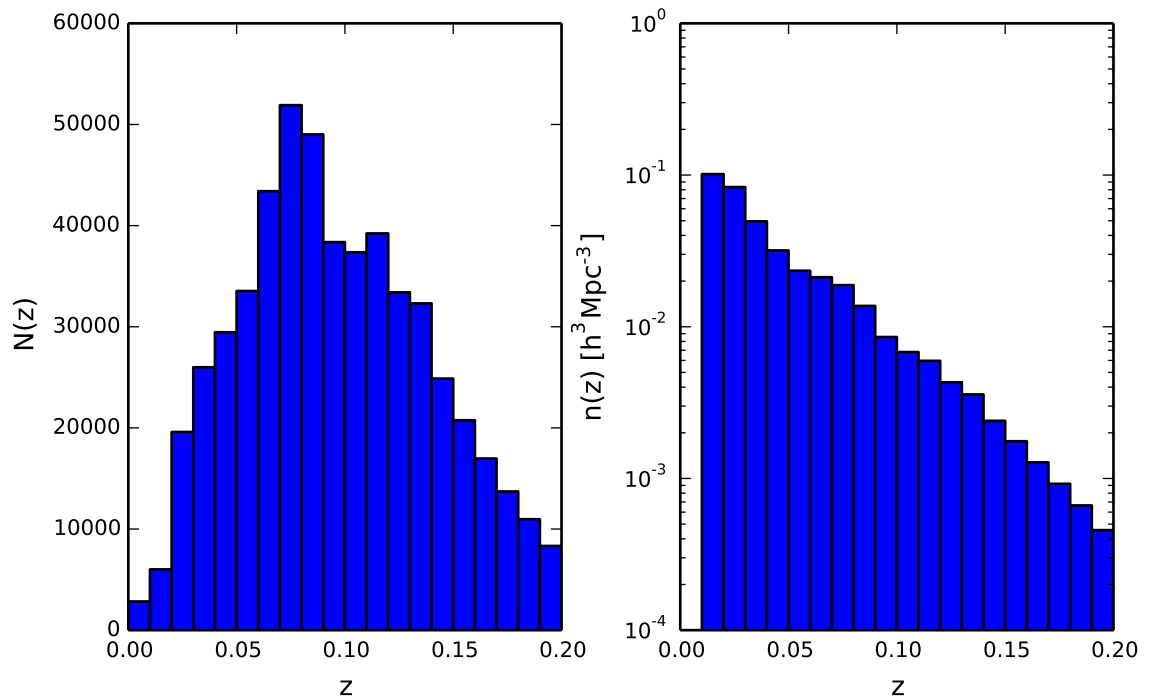


Figure 3.1: Histograms of the number (a) and number density (b) of galaxies as a function of redshift for $z < 0.20$ for the SDSS DR7 MAIN galaxy sample. Bins are of width $\Delta z = 0.01$.

and are constructed so that they have a constant surface density within the window of the survey but outside the mask. We assign random redshifts drawn from the sample's $N(z)$ to each random galaxy, and use ~ 5 times as many randoms as data points. Weights based on $n(z)$ are applied when calculating the pair counts in the sample, given by

$$w(z) = \frac{1}{1 + 4\pi n(z) J_3(s)}, \quad (3.2)$$

where $J_3(s)$ is given by

$$J_3(s) = \int_0^s \xi(s) s^2 ds. \quad (3.3)$$

Rather than recalculate $J_3(s)$ for each separation, we use assume a constant value of $4000 h^{-3} \text{ Mpc}^3$. This weighting scheme gives our sample an effective, weighted mean redshift of $z_{eff} = 0.15$.

3.3.2 Error Estimation

Due to computational constraints, we will not be making use of mock catalogues for error estimation. In lieu of this, Norberg et al. (2009) advocate the use of bootstrap sampling. This involves splitting the data into sub-areas based on their angular positions on the sky, and calculating the mean of a resampling of these sub-areas using sampling with replacement. We select $3 \times N_{sub}$ sub-areas for each resampling, where N_{sub} is the number of sub-areas created, and in total we generate $N_{boot} = 100$ resamplings of the data to calculate $\bar{\xi}$, the mean correlation function. We

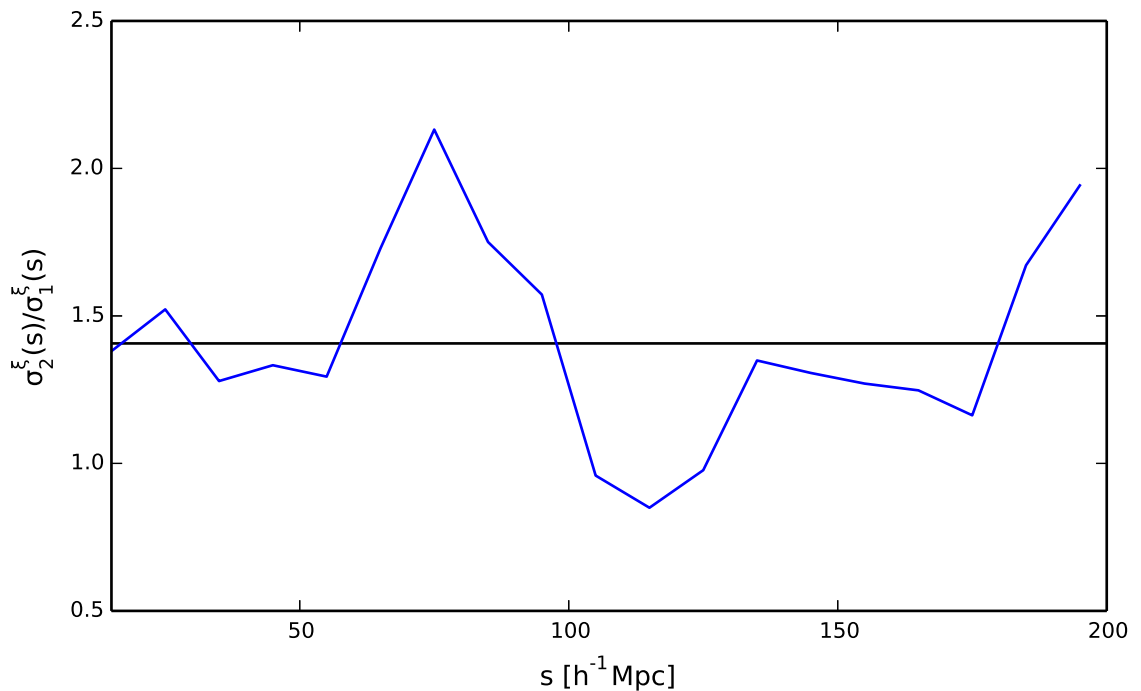


Figure 3.2: Ratio of the diagonal elements of the covariance matrices for the scheme 2 and scheme 1 subsample schemes. The solid line shows the average value, 1.45.

may then calculate a covariance matrix,

$$\mathbf{C}_{i,j} = \frac{1}{N_{boot} - 1} \sum_{n=1}^{N_{boot}} (\xi_n(s_i) - \bar{\xi}(s_i))(\xi_n(s_j) - \bar{\xi}(s_j)), \quad (3.4)$$

where ξ_n is the mean correlation function from each individual resampling, and the subscripts i and j correspond to the i th and j th redshift-space bins respectively. We choose our sub-areas such that the number density of galaxies is consistent across all samples. We make use of two different sub-areas: an average area of 830 deg^2 , giving 7 sub-areas (scheme 1); and an average area of 386 deg^2 , giving 15 sub-areas (scheme 2). From Norberg et al. we expect the diagonal terms of each covariance matrix to be consistent. This is refuted by Fig. 3.2, which shows that the ratio of the diagonal elements of scheme 2 to scheme 1 fluctuates wildly, but is mostly greater than unity, and has an average value of 1.45. This suggests that scheme 1 underestimates the errors in the sample, and so we will use scheme 2 for our error analysis.

3.3.3 Cosmological Ruler

A naive way of determining cosmological parameters is to perform a standard rod test. By comparing the observed position, in comoving coordinates, of some standard rod at different redshifts, it is possible to compare different cosmologies by shifting the position of the rod at each redshift with respect to the fiducial cosmology it was observed within, and assessing how well these shifted positions agree. We choose to compare the position of the BAO peak in our $\xi(s)$ with that in the

pre-reconstruction CMASS DR11 data (Anderson et al. 2014a), measured at $z_{eff} = 0.57$. As CMASS uses different redshift-space bins to us we instead compare our model against their best-fit cosmological model: Λ CDM with $\Omega_m = 0.274$, shifted by $\alpha = 1.031$ and normalized to our correlation function at $s \approx 50 h^{-1}$ Mpc. For each redshift-space bin we compare $\xi_{shift}(s) = \xi(s/d_{0.15})$ against $\xi_{shift}^{model}(s) = \xi^{model}(s/d_{0.57})$, where $d_z = D_C(z)/D_{C, fid}(z)$, the ratio of comoving line-of-sight distances to redshift z in the model of interest and fiducial cosmologies. We will perform chi-squared minimization over the range $0.01 \leq \Omega_m \leq 1.0$ in steps of $\Delta\Omega_m = 0.01$ (see § 3.3.4 for details of how chi-squared is calculated).

3.3.4 Model Fitting

As a more conventional approach to model fitting, we also perform a similar analysis to e.g. Xu et al. (2012). When fitting models to data, one would normally be required to determine $\xi(s)$ separately for each different cosmological model to be fitted. This is computationally expensive, so instead we define

$$\alpha = \frac{D_V(z)}{D_{V, fid}(z)} \frac{r_{d, fid}}{r_d}, \quad (3.5)$$

which corresponds to a shift in the position of the BAO peak from the fiducial model, providing the models don't differ too much. The position of the sound horizon at the drag epoch, r_d , is calculated using eq. 6 of Eisenstein & Hu (1998), and D_V combines both H_0 and D_A into a single measurement: a spherically-averaged distance to redshift z ,

$$D_V(z) \equiv \left[cz(1+z)^2 \frac{D_A(z)^2}{H(z)} \right]^{1/3}. \quad (3.6)$$

To calculate our theoretical $\xi(s)$ we follow the procedure discussed in, for example, Anderson et al. (2012). We begin by generating a linear power spectrum, $P^{lin}(k)$, using CAMB, and then calculate $P^{nw}(k)$ with the BAO feature removed, making use of the procedure discussed in Eisenstein & Hu (1998). We combine both of these spectra to produce a power spectrum with damped BAO, given by

$$P^{mod}(k) = P^{nw}(k) \left[1 + \left(\frac{P^{lin}(k)}{P^{nw}(k)} - 1 \right) e^{-\frac{1}{2}k^2 \Sigma_{nl}^2} \right], \quad (3.7)$$

where the Σ_{nl} is a factor that damps the BAO, accounting for non-linear structure formation in the model. Anderson et al. (2014a) found that Σ_{nl} scales as the inverse of the effective redshift of the sample, and so we choose to set $\Sigma_{nl} = 9.0 h^{-1}$ Mpc. We will show in § 3.4.2 that our results are insensitive to the exact value of Σ_{nl} . We may then calculate our model correlation function:

$$\xi^{mod}(s) = \int_0^\infty \frac{k^2 dk}{(2\pi)^2} P^{mod}(k) j_0(ks) e^{-k^2 a^2}. \quad (3.8)$$

When fitting models we use $\xi^{fit}(s) = B_\xi^2 \xi^{mod}(\alpha s)$, where B_ξ is some amplitude factor. We normalize $P^{mod}(k)$ to our correlation function at $s \approx 50 h^{-1}$ Mpc, ensuring that $B_\xi \approx 1$.

We explore parameter space over the ranges $0.02 < \Omega_m h^2 < 0.3$ and $0.5 < \alpha < 1.5$, while marginalizing B_ξ . For each combination of parameters we calculate the χ^2 statistic, given by

$$\chi^2 = \sum_{i,j=0}^{N_{bins}} (\xi^{fit}(s_i) - \xi^{obs}(s_i)) \mathbf{C}_{i,j}^{-1} (\xi^{fit}(s_j) - \xi^{obs}(s_j)), \quad (3.9)$$

where N_{bins} is the number of redshift-space bins and ξ^{obs} is the observed correlation function. We use this statistic to calculate the likelihood, which we assume has the form $L \propto \exp(-\chi^2/2)$, and perform markhov-chain monte-carlo analysis to find the combination of parameters that maximises the likelihood. Flat priors are assumed for the 3 free parameters. We assume $\Omega_b h^2 = 0.022$ and $n_s = 0.963$, values consistent with Planck (Planck Collabaration, Ade et al. 2014a, Planck Collabaration et al. 2014b), and we quantify the dependence of our results on these parameters in § 3.4.2.

We go on to compare our model to the neutrino dominated model from chapter 2. For this analysis we assume a fiducial model of $\Omega_m h^2 = 0.2025$, $\Omega_b h^2 = 0.0304$, $\Omega_\nu = 0.85$, and $h = 0.45$. As this model is quite different to our Λ CDM fiducial model, we must re-calculate the correlation function for our sample. In addition to comparing the neutrino model against actual data, this also serves to extend the cosmological ruler test described in § 3.3.3, as we may now test how specific cosmologies, structure formation history included, fit the data.

3.4 Results

The 2-point, spherically averaged correlation function extracted from the SDSS DR7 MAIN Galaxy Sample for the concordance cosmology is presented in Fig. 3.3, along with the fiducial model used to convert redshifts and angular positions to distances, normalised at $s \approx 50 h^{-1}$ Mpc.

Errors on the points correspond to the square root of the diagonal elements of the covariance matrix defined in Eq. 3.4. We note that the amplitude of $\xi(s)$ before the expected BAO scale serves to wash out the peak somewhat. This is discussed in further detail in Labini et al. (2009), who suggest that the MAIN sample is not ideal for such precise investigation into the galaxy distribution. The majority of their discussion concerns various volume limited samples drawn from this survey, but they note that increased sample sizes do produce similar effects to those observed here.

In the rest of this section we show the results of our cosmological standard rod test, and give our best-fit values for $\Omega_m h^2$ and α from our parameter space exploration. We go on to quantify the robustness of our results, before finally showing the results of fitting the neutrino model.

3.4.1 Cosmological Ruler

In the left panel of Fig. 3.4 we show the best-fit model for the cosmological ruler test discussed in § 3.3.3. This best-fit model has $\Omega_m = 0.5 \pm 0.28$, with a chi-squared value of $\chi^2 = 13.3$

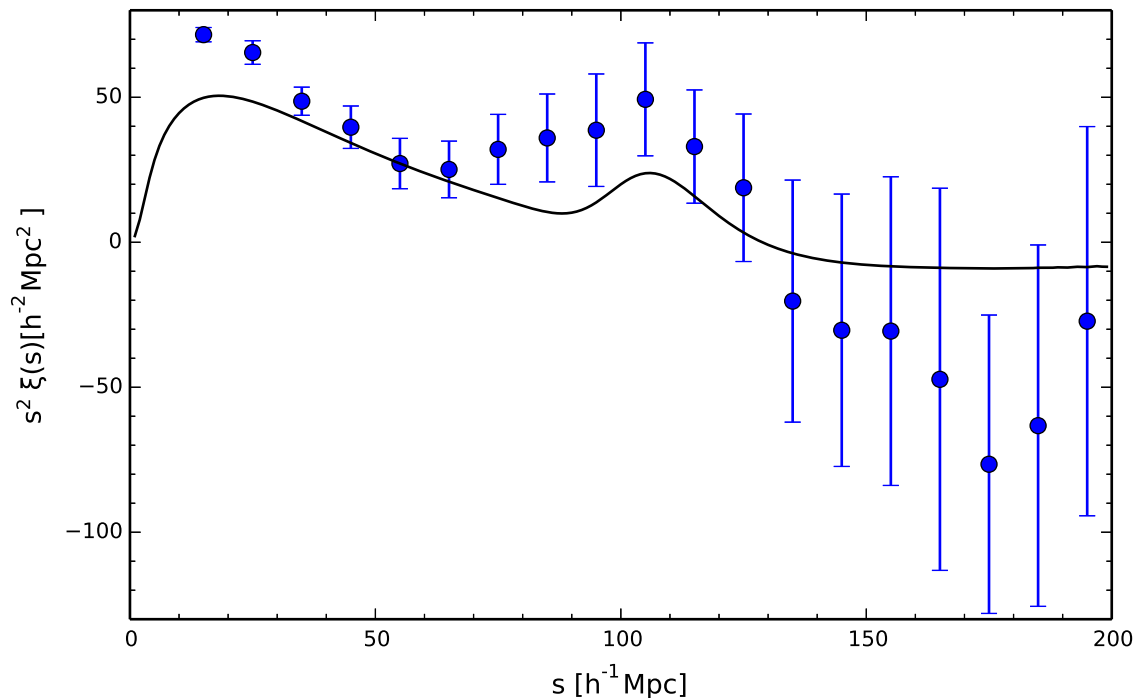


Figure 3.3: $\xi(s)$ for the SDSS DR7 MAIN Galaxy sample at $z_{eff} = 0.15$ (solid circles), along with the normalised Λ CDM fiducial model with $\Omega_m = 0.2726$, $\Omega_b = 0.0400$, $h = 0.7$.

($p = 0.65$ with 16 degrees of freedom). We display both the measured data and the shifted data, which have been shifted by $d(z_{eff})/d^{fid}(z_{eff}) = 0.98$. In the right panel we show the data shifted by $d(z_{eff})/d^{fid}(z_{eff}) = 0.93$, corresponding to $\Omega_m = 1.00$. The shifting of the peak in each case is readily apparent, but it appears that the shifted models are fit well by the corresponding shifted data, if not equally well. We quantify this in Fig. 3.5 with the chi-squared distribution about the best-fit value. These data slightly disfavour an $\Omega_m = 1$ with $\Delta\chi^2 = 2$, although using this method we cannot reject with reasonable confidence either an $\Omega_m = 1.0$ or 0.3 model as both are within 2σ of the best-fit value. These data therefore require more sophisticated methods of analysis, as discussed in § 3.3.4.

3.4.2 Parameter Exploration

In Fig. 3.6 we are able to present our best-fit model with parameters $\Omega_m h^2 = 0.142 \pm 0.012$ and $\alpha = 1.035 \pm 0.105$, and $\chi^2 = 12.8$ ($p = 0.685$ with 16 degrees of freedom). These values correspond to the median values from our markov-chain monte-carlo analysis, with errors corresponding to the 68 % confidence level from our likelihood distribution, shown in Fig. 3.7.

For a model without the BAO feature, which we approximate by setting $\Sigma_{nl} = \infty$, we find a best-fit $\Delta\chi^2 = 6.9$, which corresponds to a 2.6σ detection of the BAO peak. This low value is unsurprising given the amplitude of the correlation function just below the BAO scale, which serves to wash out the peak.

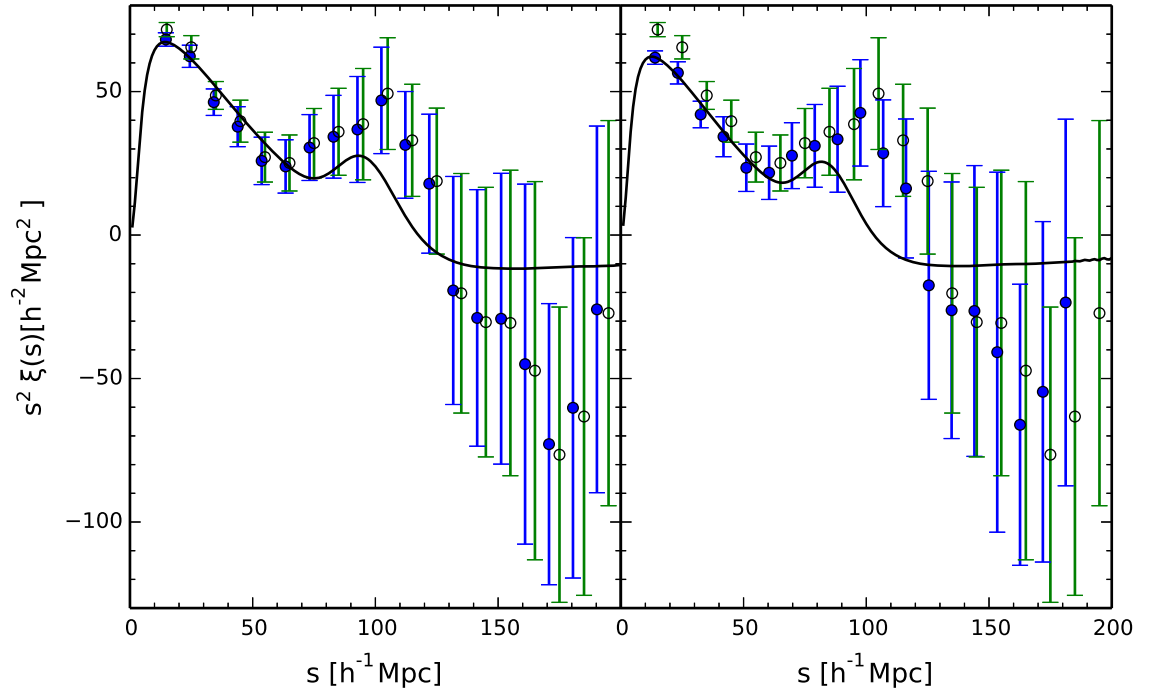


Figure 3.4: Left: the best-fit $\xi(s)$ with $\Omega_m = 0.50 \pm 0.28$ from the cosmological ruler test (solid line), along with data shifted by $d(z_{eff})/d^{fid}(z_{eff}) = 0.98$ (solid circles) and measured data (empty circles). Right: $\xi(s)$ with $\Omega_m = 1.00$ from the cosmological ruler test (solid line), along with data shifted by $d(z_{eff})/d^{fid}(z_{eff}) = 0.93$ (solid circles) and measured data (empty circles).

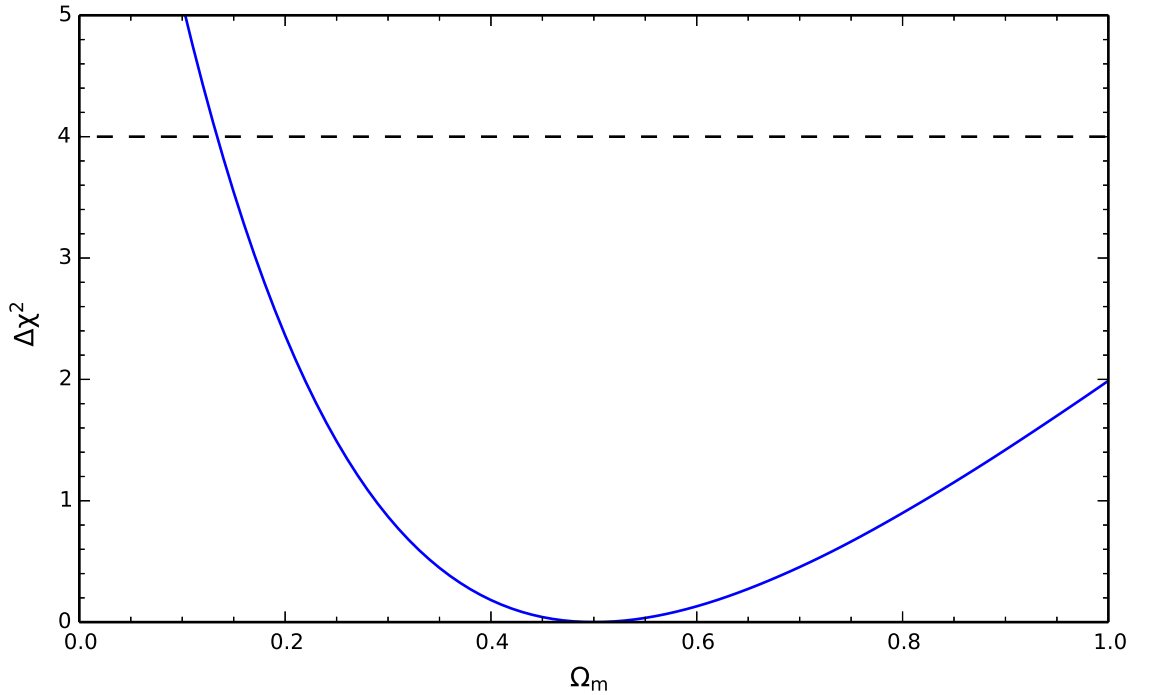


Figure 3.5: The chi-squared distribution of the cosmological ruler test about the best-fit value. The dashed line denotes 2σ .

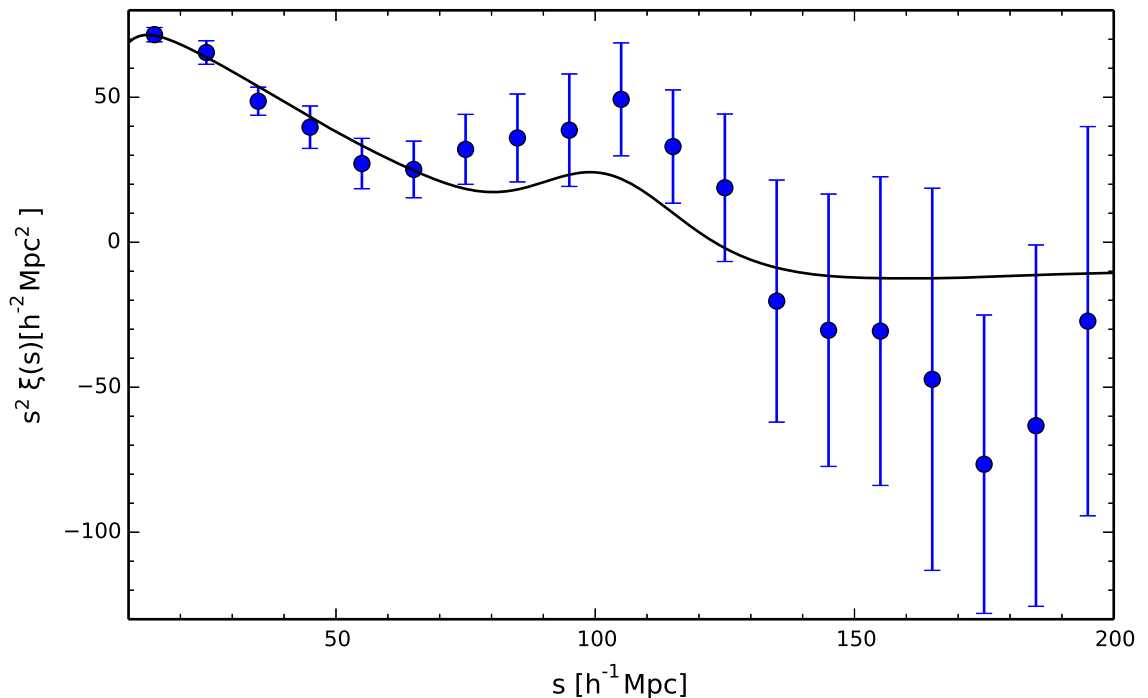


Figure 3.6: $\xi(s)$ for the SDSS DR7 MAIN Galaxy sample at $z_{eff} = 0.15$ (solid circles), along with the best-fit concordance cosmology with parameters $\alpha = 1.035 \pm 0.105$ and $\Omega_m h^2 = 0.142 \pm 0.013$ (solid line).

Robustness Checks

The errors on these two best-fit parameters are reasonable (< 10 per cent), which is surprising given the broadness of the peak recovered from our sample. We test our error estimation by performing this same analysis procedure, but only using the diagonal covariance matrix terms for our χ^2 calculation. This reduces the measured χ^2 to 12.2, and changes the model parameters to $\Omega_m h^2 = 0.141 \pm 0.012$ and $\alpha = 1.033 \pm 0.106$, a less than 1 per cent shift in each case, which raises our confidence in our error estimation.

We further quantify the robustness of our results by changing Σ_{nl} , $\Omega_b h^2$ and n_s as outlined in

Table 3.1: Robustness checks performed on our measurements of α and $\Omega_m h^2$. We vary three parameters: Σ_{nl} , $\Omega_b h^2$, and n_s , and truncate the range of s bins used in our analysis, and record the different values for α and $\Omega_m h^2$ measured along with the χ^2 statistic for the new combination of parameters.

Robustness Check	$\Omega_m h^2$	α	χ^2
$\Sigma_{nl} = 8.0 h^{-1} \text{ Mpc}$	0.144 ± 0.013	1.035 ± 0.103	13.3
$\Omega_b h^2 = 0.032$	0.169 ± 0.010	0.944 ± 0.070	11.4
$n_s = 1.62$	0.127 ± 0.010	1.056 ± 0.091	11.2
$40 < s < 160 h^{-1} \text{ Mpc}$	0.101 ± 0.016	1.142 ± 0.125	6.0

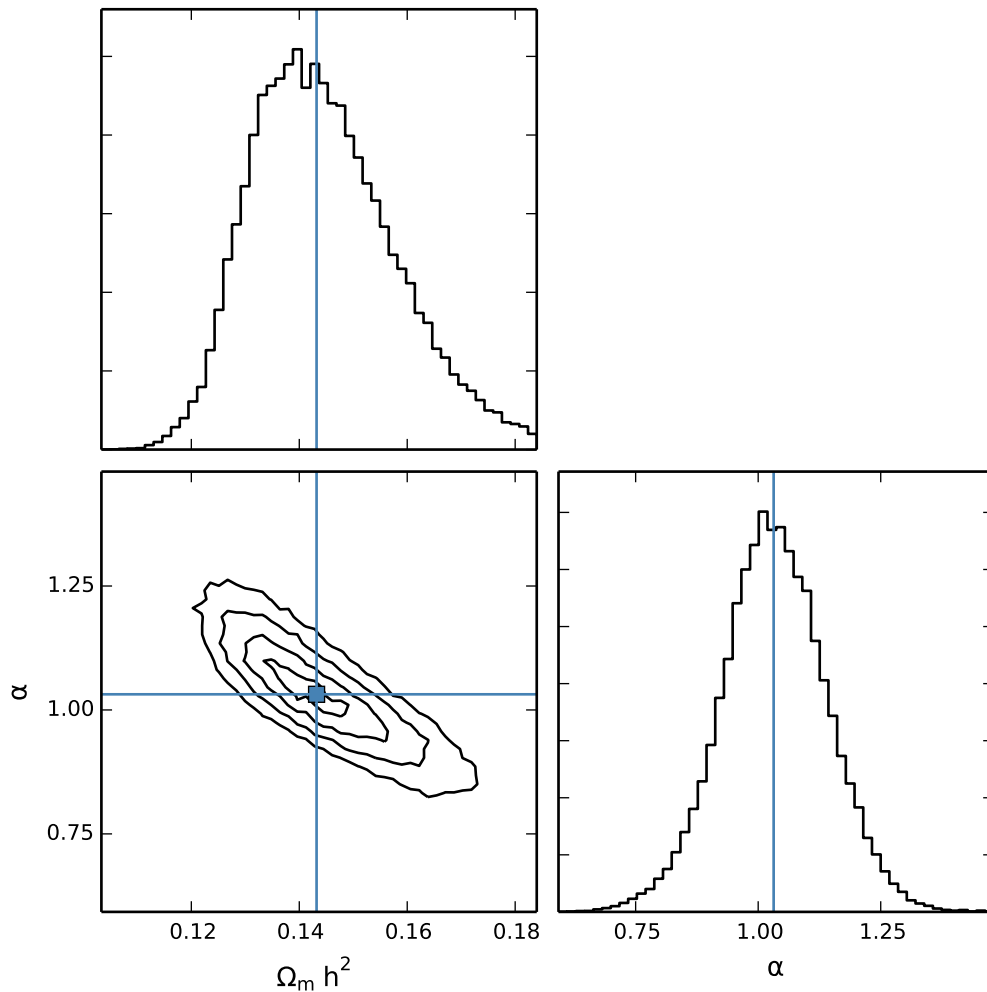


Figure 3.7: Likelihood contours for the parameters $\Omega_m h^2$ and α are shown in the bottom-left plot, and the probabilities associated with each parameter in the lower-right and upper plots. The best fit values are located at the intersection of the vertical and horizontal lines in the contour plot, and the vertical lines on the diagonal plots. Contours correspond to $1-4\sigma$.

Table 3.1. We plot the best-fit models of the tests carried out in Fig. 3.8.

Our results are most robust to changes in Σ_{nl} : both $\Omega_m h^2$ and α change by less than 1 per cent, and the data slightly disfavour this lower Σ_{nl} with $\Delta\chi^2 = 0.5$. Varying the other two parameters produces greater changes in both the best-fit $\Omega_m h^2$ and α and the χ^2 for said fit. Varying $\Omega_b h^2$ by ≈ 45 per cent produces shifts of 19 and 9 per cent respectively in $\Omega_m h^2$ and α , while changing n_s by 10 per cent produces changes of 11 and 2 per cent. Both of these changes are better accepted by the data, with $\Delta\chi^2 \approx -1.4$ and $\Delta\chi^2 \approx -1.6$ for changes in $\Omega_b h^2$ and n_s respectively. The best-fit models for both enjoy slight increases in the amplitude of the BAO peak, but at larger scales are much the same as the best-fit to the concordance cosmology. From these checks we determine that the best-fit parameters are not strongly dependent on $\Omega_b h^2$ or Σ_{nl} , but that there is appreciable dependence of $\Omega_m h^2$ on n_s , and that $\Omega_m h^2$ is the more weakly constrained of the

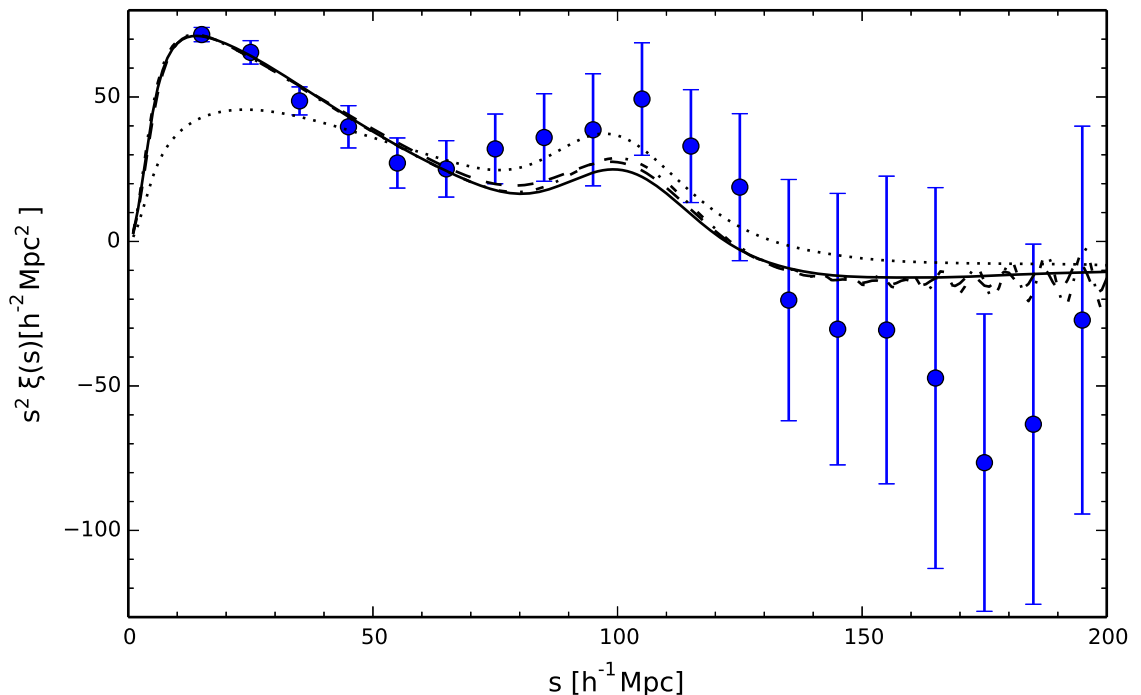


Figure 3.8: The best-fit models for each of the robustness checks on $\xi(s)$. Filled circles represent the measured $\xi(s)$. The solid line shows $\Sigma_{nl} = 8.0 h^{-1} \text{ Mpc}$; the dashed line shows $\Omega_b h^2 = 0.032$; the dash-dot line shows $n_s = 1.062$; the dotted line shows the best fit model for bins $40 < s < 160 h^{-1} \text{ Mpc}$.

two cosmological parameters.

Finally, we test how constrained the best-fit parameters are by the detection of the BAO peak by considering bins between $40 < s < 160 h^{-1} \text{ Mpc}$, also shown in Fig. 3.8. Doing so changes the best-fit cosmological model considerably: $\alpha = 1.142 \pm 0.125$ and $\Omega_m h^2 = 0.102 \pm 0.016$. This lower $\Omega_m h^2$ increases the amplitude of $\xi(s)$ about the peak, as well as broadening it, which matches the data more closely than the best-fit model using the full range ($\chi^2 = 6.0$ with 9 degrees of freedom). This goes against findings from many other sources, which suggest that the position and amplitude of the peak are enough to constrain the cosmological model. We therefore conclude that our best-fit parameters, even though they are a reasonable fit to the data, are constrained more by the overall shape of the correlation function than the presence of the BAO peak, although the peak is still detected at 2.2σ ($\Delta\chi^2 = 4.8$).

3.4.3 Neutrino Cosmology

The correlation function extracted from the SDSS DR7 MAIN Galaxy Sample for the neutrino cosmology is presented in Fig. 3.9, along with the fiducial model used to convert redshifts and angular positions to distances, normalised at $s \approx 50 h^{-1} \text{ Mpc}$.

We obtain a value for the chi-squared statistics for the neutrino model over all redshift bins of $\chi^2 = 964.3$. This poor fit is in large part a result of the low- s bins, which are dominated by

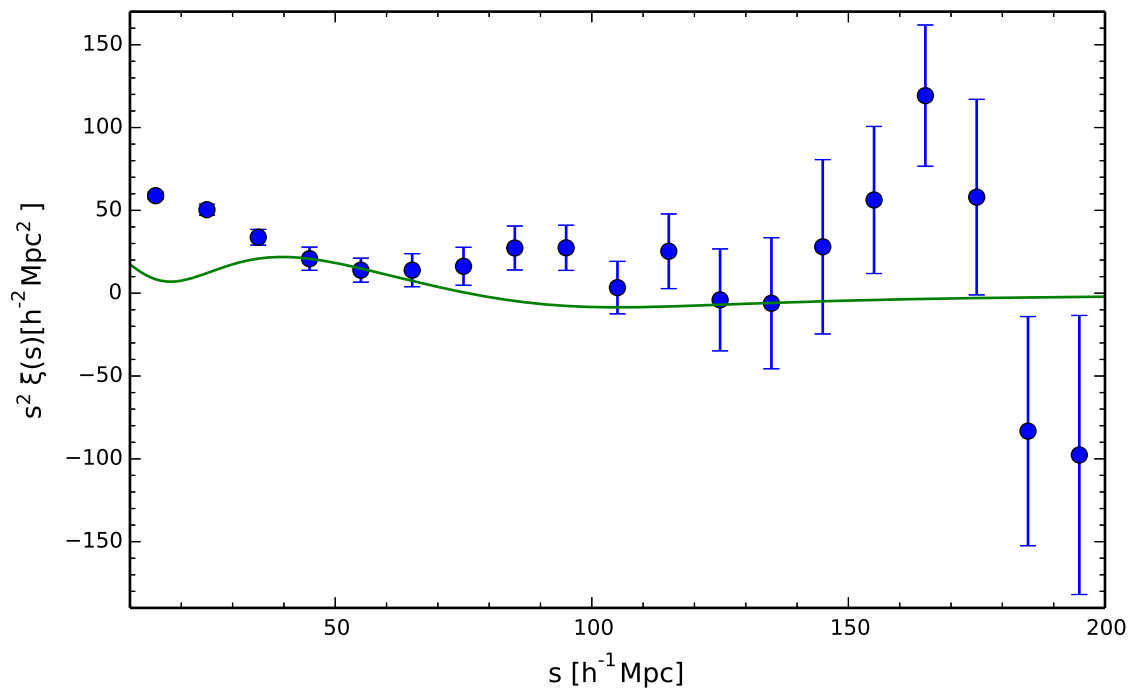


Figure 3.9: $\xi(s)$ for the SDSS DR7 MAIN Galaxy sample at $z_{eff} = 0.15$ (solid circles), along with the normalised neutrino fiducial model with $\Omega_\nu = 0.85$, $\Omega_b = 0.15$, $h = 0.45$.

non-linear effects not accurately accounted for in this model (see chapter 2). If the low- s bins are excluded, and we instead examine the fit due to the large-scale clustering of galaxies, we obtain a substantially smaller chi-squared value of $\chi^2 = 39.8$.

3.5 Discussion

Assuming our fiducial cosmology of $\Omega_m = 0.273$, $\Omega_b = 0.040$, $\Omega_\Lambda = 0.727$ and $H_0 = 70 \text{ km s}^{-1} \text{ Mpc}^{-1}$, we have $D_{V, fid}(0.15) = 606.294 \text{ Mpc}$, and $r_{s, fid} = 146.56 \text{ Mpc}$. We therefore measure the spherically averaged distance to $z = 0.15$ as

$$D_V(0.15) = (627 \pm 61 \text{ Mpc}) \left(\frac{r_s}{r_{s, fid}} \right), \quad (3.10)$$

and the ratio $D_V(0.15)/r_d = 4.28 \pm 0.42$. We use our best-fit $\Omega_m h^2$ to calculate $r_d = 152 \pm 4 \text{ h}^{-1} \text{ Mpc}$, and therefore our best-fit spherically averaged distance to $z = 0.15$ is $D_V(0.15) = 648 \pm 66 \text{ h}^{-1} \text{ Mpc}$.

This is in agreement with the recent study by Ross et al. (2014), who measure the correlation function and power spectrum for those galaxies with $M_r < -21.2$ in the MAIN galaxy sample. They present a best-fit ratio $D_V(0.15) = (664 \pm 25 \text{ Mpc}) \left(\frac{r_s}{r_{s, fid}} \right)$. This is a more precise result than that presented here, due to their use of reconstruction techniques to sharpen their BAO peak. When comparing to their pre-reconstruction, $\xi(s)$ only measurement, we find

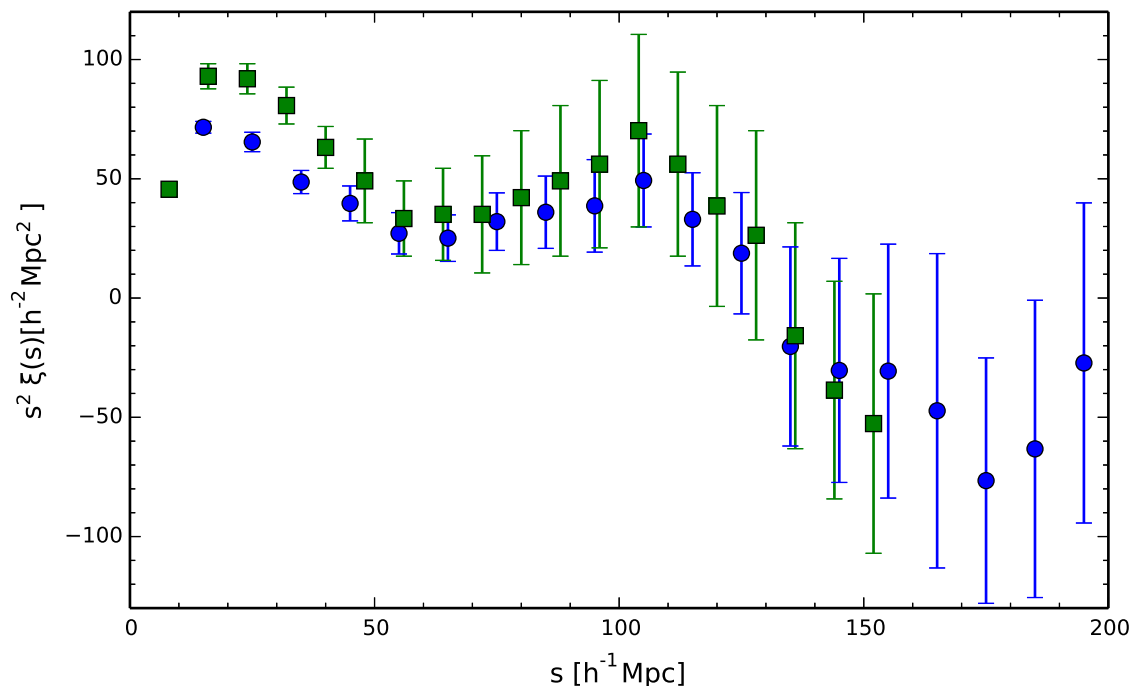


Figure 3.10: The measured correlation function from the MAIN galaxy sample for this study (blue circles) and the pre-reconstruction $\xi(s)$ from Ross et al. (2014) (green squares).

that their error on α approaches that of ours (± 0.094), demonstrating the potential power of reconstruction when obtaining fits. This shows strongest when determining how much the BAO peak constrains the cosmological parameters measured: when Ross et al. (2014) use only bins between $50 < s < 150 h^{-1} \text{ Mpc}$ they measure $\alpha = 1.057 \pm 0.037$, a shift of only 0.1 per cent (cf. § 3.4.2). The final point worth mentioning about these two studies is that the errors on $\xi(s)$ for their pre-reconstruction correlation function are larger than ours until after the BAO scale, as shown in Fig. 3.10. We attribute this to their exclusion of fainter galaxies in their sample, which cuts their sample size by a factor ≈ 10 . This suggests that a full study of the MAIN galaxy sample is still warranted, and that application of reconstruction etc. to the full sample could still shed light on the expansion history of the universe.

Our best-fit $\Omega_m h^2$ is consistent with the Planck (Planck Collaboration et al. 2014b) best-fit ΛCDM cosmology, which has $\Omega_m h^2 = 0.14300$ (68 per cent limits $\Omega_m h^2 = 0.1423 \pm 0.0029$), and $D_V(0.15)/r_d = 4.212 \pm 0.011$, which we calculate by drawing $\Omega_c h^2$, $\Omega_b h^2$ and H_0 from gaussian priors centered on the best-fit Planck+WMAP ΛCDM model. We display our result, along with Ross et al. (2014), in Fig. 3.11. We also plot results from other key studies: 6dFGS (Beutler et al. 2011), at $z = 0.106$; BOSS DR11 LOWZ and CMASS (Anderson et al. 2014a) at $z = 0.32$ and 0.57 respectively; Percival et al. (2010) at $z = 0.275$; WiggleZ (Kazin et al. 2014) at $z = 0.44$, 0.6 , and 0.73 ; and Chuang et al. (2012) at $z = 0.15$, who use the DR7 LRG data to determine $D_V(0.35)$. The 6dFGS and SDSS surveys have little overlap - only LOWZ covers the SGC at that

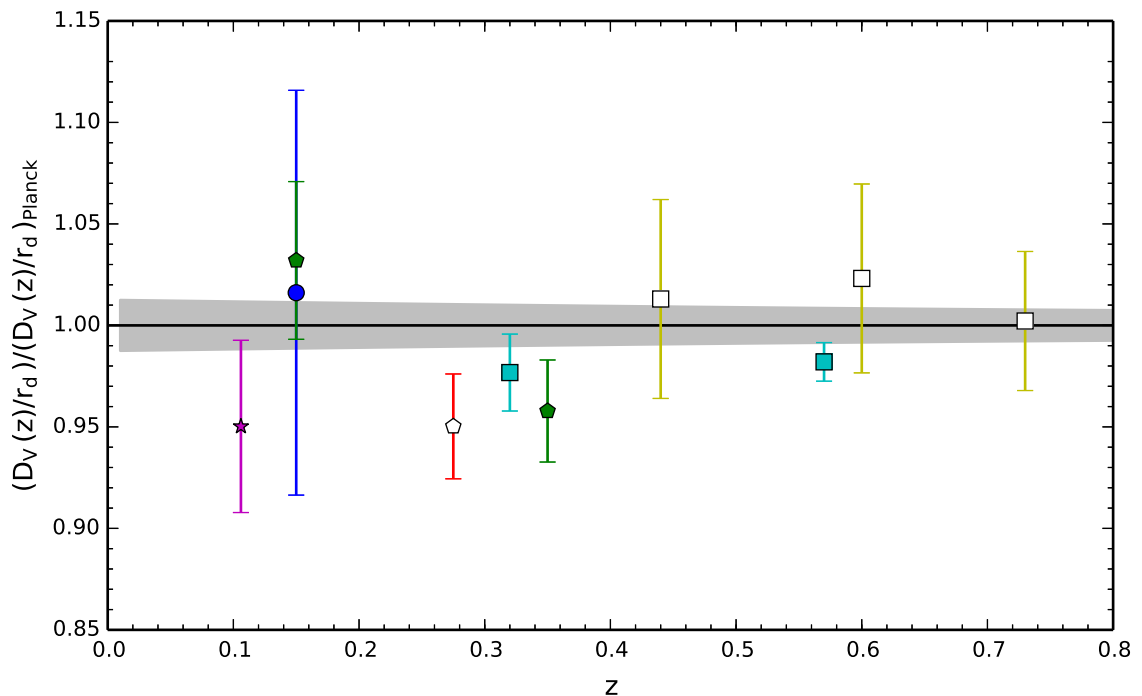


Figure 3.11: Ratio of $D_V(z)/r_d$ against the best-fit Planck + WMAP predictions for various studies. The line at 1 is the Planck ratio by construction, and shaded areas show 1σ spread of $(D_V(z)/r_d)_{Planck}$, determined through sampling $\Omega_c h^2$, $\Omega_b h^2$ and H_0 from gaussians centered on the Planck + WMAP best-fit values. The solid circle denotes the value from this study; the open pentagon shows the Percival et al. (2010) DR7 value; solid pentagons show DR7 values for the MAIN galaxy sample and the LRG sample; solid squares denote DR11 BOSS CMASS and LOWZ values; open squares show WiggleZ values; and the star denotes the 6dFGS value.

redshift - and the DR7 MAIN sample is completely independent of 6dFGS, BOSS CMASS and WiggleZ, but does overlap BOSS LOWZ.

We note that $D_V(0.15)/r_d$ for the SDSS MAIN galaxies at $z = 0.15$ are greater than the Planck values, whereas the other DR7 $D_V(z)/r_d$ values are lower than Planck predictions. This must stem from the inclusion of LRGs in each sample, as these other DR7 studies are not independent of each other, either in terms of volume or sample. However, the large errors on α measured in this sample do allow for $(D_V(z)/r_d)/(D_V(z)/r_d)_{Planck} < 1$; it would be interesting to investigate what effect reconstruction and the use of mocks for error estimation would have on the full MAIN sample correlation function, and whether $D_V(z)/r_d$ measured after application of these methods would also remain greater than Planck predictions.

Finally, although our data preferred $\Omega_b h^2 = 0.032$ and $n_s = 1.062$ in the robustness checks, these values are ruled out by Planck at greater than 30σ and 10σ respectively, and so are not included in our best-fit parameters.

3.5.1 Alternate Cosmological Models

When performing the cosmological ruler test, we examined only the effect Ω_m had on the distance scale. This proved ineffective in distinguishing between different cosmological models, as detailed structure formation histories were not taken into account. For example, while in this test $\Omega_m = 0.3$ and 1 were in agreement to $< 2\sigma$, the parameter exploration, which takes into account Λ and its effect on the power spectrum, rejects an $\Omega_m = 1$ model at $\gg 4\sigma$, as shown by Fig. 3.7. However, this is not due to the presence of the BAO peak. Removing the low- s bins from the analysis of the neutrino model improves the fit by almost two orders of magnitude, and these bins are dominated by non-linear effects anyway (although the magnetic neutrino models did produce some structure). While the best results of the paper are those presented above, we conclude by saying that these data do not rule out higher Ω_m models conclusively.

Chapter 4

Conclusion

The goal of this paper was to examine the differences between Einstein-de Sitter, HDM models and the standard Λ CDM model, through investigations into the large-scale clustering of matter in the universe. To that end, we performed a suite of N -body simulations of a neutrino dominated model, described by parameters $\Omega_\nu = 0.85$, $\Omega_n = 0.15$ and $h = H_0 / 100 \text{ km s}^{-1} \text{ Mpc}^{-1} = 0.45$. We observed the Halo Mass Function of the model and the evolution over time of the power spectrum, and found that unless $P(k)$ is unphysically normalized to greater amplitudes, no structure can form by the present day. The structure found in these renormalized models is primarily spurious in nature, accounting for the non-linearities observed in the power spectra of these models at low redshifts, but when this is taken into account the HMF produced display the characteristic plateau at intermediate masses, caused by the collapse of pancake-like structures into large-mass halos - the top-down picture of structure formation.

The introduction of Primordial Magnetic Fields, generated in the very early universe, but too weak to play a direct role in structure formation at the present day, provide a natural way of seeding HDM models with structure. This causes the models to form structure in a bottom-up manner, as in Λ CDM, but the problems inherent in such picture of structure formation are exacerbated here: the low-mass end of the HMF has a far greater amplitude than Λ CDM, and the high-mass end lags considerably behind Λ CDM predictions. This is most likely due to the late beginnings of structure formation in such a model when compared to Λ CDM, and as galaxies have been observed past $z = 2$, we again must conclude that such a model cannot accurately describe the observed universe.

Our investigation of the SDSS DR7 MAIN galaxy sample determined again that a Λ CDM model is a better fit to observations. Although a naive cosmological rod test suggested that our data could not reliably favour either a $\Omega_m = 1$ or 0.3 model, a parameter-space exploration rejects a neutrino HDM model at $\Delta\chi^2 > 900$, and provides best-fit values of $\alpha = 1.035 \pm 0.105$ and $\Omega_m h^2 = 0.142 \pm 0.013$. However, this rejection comes primarily from small scale clustering, dominated by non-linear effects; the performance of a hot dark matter model on such scales is

already known to be poor (despite the magnetic models producing appreciable quantities of structure). Excluding these bins, we find that the fit to the neutrino model is improved by almost two orders of magnitude. This is a relative success for a hot dark matter model, considering that these large scales are where *Lambda*CDM models excel.

We present a best-fit spherically-averaged distance to $z = 0.15$ of $D_V(0.15) = (627 \pm 61\text{Mpc}) \left(\frac{r_s}{r_{s, fid}} \right)$, which is in agreement with the recent study by Ross et al. (2014), who measure the power spectra and correlation function from the same sample.

We detect the BAO peak at 2.6σ : this low significance is similar to Ross et al. (2014), who recover $\alpha = 1.013 \pm 0.094$ for their pre-reconstructed sample. The size of their errors in this sample compared to ours suggests that, if our error estimates are accurate, a full investigation of the SDSS DR7 Main galaxy survey, including as many galaxies as possible, coupled with the reconstruction methods utilized by Ross et al. (2014) and others, would provide valuable insight into the nature of the universe at $z = 0.15$.

Ultimately, we find that the concordance cosmology is the best-fit to our data. Our work here serves to highlight many of the difficulties faced by any alternative cosmological model when dealing with the large-scale structure of the universe, where the Λ CDM model remains strongest.

Bibliography

- Abazajian, N. K. et al. (2009), ‘The seventh data release of the sloan digital sky survey’, *ApJS* **182**, 543.
- Anderson, L. et al. (2012), ‘The clustering of galaxies in the sdss-iii baryon oscillation spectroscopic survey: baryon acoustic oscillations in the data release 9 spectroscopic galaxy sample’, *MNRAS* **427**, 3435.
- Anderson, L. et al. (2014a), ‘The clustering of galaxies in the sdss-iii baryon oscillation spectroscopic survey: Baryon acoustic oscillations in the data release 10 and 11 galaxy samples’, *MNRAS* **441**, 24.
- Anderson, L. et al. (2014b), ‘The clustering of galaxies in the sdss-iii baryon oscillation spectroscopic survey: including covariance matrix errors’, *MNRAS* **439**, 2531.
- Angus, G. W. (2009), ‘Is an 11 ev sterile neutrino consistent with clusters, the cosmic microwave background and modified newtonian dynamics?’, *MNRAS* **394**, 527.
- Aseev, V. N. et al. (2011), ‘Upper limit on the electron antineutrino mass from the troitsk experiment’, *Phys. Rev. D* **84**.
- Baugh, C. M. et al. (2005), ‘Can the faint submillimetre galaxies be explained in the cold dark matter model?’, *MNRAS* **356**, 1191.
- Benson, A. J. et al. (2003), ‘What shapes the luminosity function of galaxies?’, *ApJ* **599**, 38.
- Beutler, F. et al. (2011), ‘The 6df galaxy survey: Baryon acoustic oscillations and the local hubble constant’, *MNRAS* **416**, 3017.
- Blanton, M. R. et al. (2005), ‘New york university value-added galaxy catalog: A galaxy catalog based on new public surveys’, *AJ* **129**, 2562.
- Bode, P. et al. (2001), ‘Halo formation in warm dark matter models’, *ApJ* **556**, 93.
- Bower, R. G. et al. (2006), ‘Breaking the hierarchy of galaxy formation’, *MNRAS* **370**, 645.
- Carlesi, E. et al. (2012), ‘N-body simulations with a cosmic vector for dark energy’, *MNRAS* **424**.
- Chaboyer, B. (1998), ‘The age of the universe’, *Physics Reports* **307**, 23.

- Chuang, C. H. & Wang, Y. (2013), ‘Modelling the anisotropic two-point galaxy correlation function on small scales and single-probe measurements of $h(z)$, $d_a(z)$ and $f(z)\sigma_8(z)$ from the sloan digital sky survey dr7 luminous red galaxies’, *MNRAS* **435**, 255.
- Chuang, C. H., Wang, Y. & Hemantha, M. D. P. (2012), ‘A robust distance measurement and dark energy constraints from the spherically averaged correlation function of sloan digital sky survey luminous red galaxies’, *MNRAS* **423**, 1474.
- Cole, S. et al. (2005), ‘The 2df galaxy redshift survey: power-spectrum analysis of the final data set and cosmological implications’, *MNRAS* **362**, 205.
- Coles, P. (1992), ‘Primordial magnetic fields and the large-scale structure of the universe’, *Comments Astrophys.* **16**.
- Colín, P. et al. (2008), ‘Halo mass function and the free streaming scale’, *ApJ* **673**, 203.
- Colombi, S. et al. (2009), ‘Accurate estimators of power spectra in n-body simulations’, *MNRAS* **393**, 511.
- Dawson, K. S. et al. (2013), ‘The baryon oscillation spectroscopic survey of sdss-iii’, *AJ* **145**, 10.
- Dehnen, W. (2001), ‘Towards optimal softening in three-dimensional n-body codes - i. minimizing the force error’, *MNRAS* **324**, 273.
- Eisenstein, D. J. & Hu, W. (1998), ‘Baryonic features in the matter transfer function’, *ApJ* **496**, 605.
- Eisenstein, D. J. et al. (2005), ‘Detection of the baryon acoustic peak in the large-scale correlation function of sdss luminous red galaxies’, *ApJ* **633**, 560.
- Eisenstein, D. J. et al. (2011), ‘Sdss-iii: Massive spectroscopic surveys of the distant universe, the milky way, and extra-solar planetary systems’, *AJ* **142**, 72.
- Foreman-Mackey, D. et al. (2013), ‘emcee: The mcmc hammer’, *PASP* **125**, 306.
- Frenk, C. S. & White, S. D. M. (2012), ‘Dark matter and cosmic structure’, *Annalen der Physik* **524**, 507.
- Frieman, J. A. et al. (2008), ‘The sloan digital sky survey-ii supernova survey: Technical summary’, *AJ* **135**, 338.
- Jenkins, A. et al. (2001), ‘The mass function of dark matter haloes’, *MNRAS* **321**, 372.
- Kahniashvili, T. et al. (2013), ‘Constraining primordial magnetic fields through large-scale structure’, *ApJ* **770**.

- Kazin, E. A. et al. (2014), ‘The wigglez dark energy survey: improved distance measurements to $z=1$ with reconstruction of the baryonic acoustic feature’, *MNRAS* **441**, 3524.
- Klypin, A. et al. (1993), ‘Structure formation with cold plus hot dark-matter’, *ApJ* **416**, 1.
- Klypin, A. et al. (1999), ‘Where are the missing galactic satellites?’, *ApJ* **522**, 82.
- Knebe, A. et al. (2003), ‘Top-down fragmentation of a warm dark matter filament’, *MNRAS* **345**, 1285.
- Labini, F. S. et al. (2009), ‘Absence of anti-correlations and of baryon acoustic oscillations in the galaxy correlation function from the sloan digital sky survey data release 7’, *A&A* **505**, 981.
- Landy, S. D. & Szalay, A. S. (1993), ‘Bias and variance of angular-correlation functions’, *ApJ* **412**, 64.
- Lewis, A., Challinor, A. & Lasenby, A. (2000), ‘Efficient computation of cosmic microwave background anisotropies in closed friedmann-robertson-walker models’, *Astrophysical Journal* **538**, 473.
- Manera, M. et al. (2013), ‘The clustering of galaxies in the sdss-iii baryon oscillation spectroscopic survey: a large sample of mock galaxy catalogues’, *MNRAS* **428**, 1036.
- Manera, M. et al. (2014), The clustering of galaxies in the sdss-iii baryon oscillation spectroscopic survey: mock galaxy catalogues for the low-redshift sample. in press (ArXiv:1401.4171).
- Marchesini, D. et al. (2009), ‘The evolution of the stellar mass function of galaxies from $z = 4.0$ and the first comprehensive analysis of its uncertainties: Evidence for mass-dependent evolution’, *ApJ* **701**.
- Milgrom, M. (1983), ‘A modification of the newtonian dynamics as a possible alternative to the hidden mass hypothesis’, *ApJ* **270**, 365.
- Moore, B. et al. (1999), ‘Dark matter substructure within galactic halos’, *ApJ* **524**, L19.
- Navarro, J. F. et al. (1997), ‘A universal density profile from hierarchical clustering’, *ApJ* **490**, 493.
- Norberg, P. et al. (2009), ‘Statistical analysis of galaxy surveys i. robust error estimation for two-point clustering statistics’, *MNRAS* **396**, 19.
- Ostriker, J. P. & Peebles, P. J. E. (1973), ‘A numerical study of the stability of flattened galaxies; or, can cold galaxies survive?’, *ApJ* **186**, 467.
- Ostriker, J. P., Peebles, P. J. E. & Yahil, A. (1974), ‘The size and mass of galaxies, and the mass of the universe’, *ApJ* **193**, L1.

- Padmanabhan, N. et al. (2008), ‘An improved photometric calibration of the sloan digital sky survey imaging data’, *ApJ* **674**, 1217.
- Pâris, I. et al. (2012), ‘The sloan digital sky survey quasar catalog: ninth data release’, *A&A* **548**, A66.
- Peebles, P. J. E. (1974), ‘The nature of the distribution of galaxies’, *A&A* **32**, 197.
- Peebles, P. J. E. (1980), *The Large-scale Structure of the Universe*, Princeton University Press.
- Peebles, P. J. E. & Yu, J. T. (1970), ‘Primeval adiabatic perturbation in an expanding universe’, *ApJ* **162**, 815.
- Percival, W. J. et al. (2010), ‘Baryon acoustic oscillations in the sloan digital sky survey data release 7 galaxy sample’, *MNRAS* **401**, 2148.
- Perlmutter, S. et al. (1999), ‘Measurements of omega and lambda from 42 high-redshift supernovae’, *ApJ* **517**, 565.
- Planck Collaboration, Ade, P. A. R. et al. (2014a), ‘Planck 2013 results. i. overview of products and scientific results’, *A&A* **571**, A1.
- Planck Collaboration, Ade, P. A. R. et al. (2014b), ‘Planck 2013 results. xvi. cosmological parameters’, *A&A* **571**, A16.
- Power, C. (2013), ‘Seeking observable imprints of small-scale structure on the properties of dark matter haloes’, *PASA* **30**, e053.
- Riess, A. G. et al. (2011), ‘A 3% solution: Determination of the hubble constant with the hubble space telescope and wide field camera 3’, *ApJ* **730**.
- Ross, A. J. et al. (2014), The clustering of the sdss dr7 main galaxy sample i: A 4 per cent distance measure at $z=0.15$. in press (ArXiv:1409.3242).
- Schmidt, B. P. et al. (1998), ‘The high- z supernova search: Measuring cosmic deceleration and global curvature of the universe using type ia supernovae’, *ApJ* **507**, 46.
- Schneider, A. et al. (2013), ‘Halo mass function and the free streaming scale’, *MNRAS* **433**, 1573.
- Shanks, T. et al. (2014), ‘A neutrino model fit to the cmb power spectrum’, *MNRAS* **445**, 2836.
- Shaw, J. R. & Lewis, A. (2010), ‘Massive neutrinos and magnetic fields in the early universe’, *Phys. Rev. D* **81**, 043517.
- Shaw, J. R. & Lewis, A. (2012), ‘Constraining primordial magnetism’, *Phys. Rev. D* **86**.
- Shibusawa, Y. et al. (2014), ‘The influence of primordial magnetic fields on the spherical collapse model in cosmology’, *JCAP* **8**.

- Springel, V. (2005), 'The cosmological simulation code gadget-2', *Monthly Notices of the Royal Astronomical Society* **364**, 1105.
- Springel, V. et al. (2001), 'Populating a cluster of galaxies - i. results at $z=0$ ', *MNRAS* **328**, 726.
- Sunyaev, R. A. & Zel'dovich, Y. B. (1970), 'Small-scale fluctuations of relic radiation', *ApSS* **7**, 3.
- Wang, J. & White, S. D. M. (2007), 'Discreteness effects in simulations of hot/warm dark matter', *MNRAS* **380**, 93.
- Wang, J. & White, S. D. M. (2009), 'Are mergers responsible for universal halo properties?', *MNRAS* **396**, 709.
- Warren, M. S. et al. (2006), 'Precision determination of the mass function of dark matter halos', *Astrophysical Journal* **646**, 881.
- Wasserman, I. (1978), 'On the origins of galaxies, galactic angular momenta, and galactic magnetic fields', *ApJ* **224**.
- Weinberg, S. (1989), 'The cosmological constant problem', *Rev. Modern Phys.* **61**.
- Xu, X. et al. (2012), 'A 2 per cent distance to $z = 0.35$ by reconstructing baryon acoustic oscillations ii. fitting techniques', *MNRAS* **427**, 2146.
- Zehavi, I. et al. (2011), 'Galaxy clustering in the completed sdss redshift survey: The dependence on color and luminosity', *ApJ* **736**, 59.
- Zwicky, F. (1933), 'Die rotverschiebung von extragalaktischen nebeln', *Helvetica Physica Acta* **6**, 110.